ABSTRACT

Title of Document: DESIGN AND PACKAGING OF AN IRON-GALLIUM (GALFENOL) NANOWIRE ACOUSTIC SENSOR FOR UNDERWATER APPLICATIONS

Rupal Jain, Master of Science, 2007

Directed By: Associate Professor F. Patrick McCluskey, Department of Mechanical Engineering

A novel acoustic sensor incorporating cilia-like nanowires made of magnetostrictive iron-gallium (Galfenol) alloy has been designed and fabricated using micromachining techniques. The sensor and its package design are analogous to the structural design and the transduction process of a human-ear cochlea. The nanowires are sandwiched between a flexible membrane and a fixed membrane similar to the cilia between basilar and tectorial membranes in the cochlea. The stress induced in the nanowires due to the motion of the flexible membrane in response to acoustic waves results in a change in the magnetic flux in the nanowires. These changes in the magnetic flux are converted into electrical voltage changes by a GMR (giant magnetoresistive) sensor. As the acoustic sensor is designed for underwater applications, packaging is a key issue for the effective working of this sensor. A good package should provide a suitably protective environment to the sensor, while allowing sound waves to reach the sensing element with a minimal attenuation. In this thesis, design efforts aimed at producing this MEMS bio-inspired acoustic transducer have been detailed along with the process sequence for its fabrication. Package materials including encapsulants and filler fluids have been identified based on

their acoustic performance in water by conducting several experiments to compare their impedance and attenuation characteristics and moisture absorption properties. Preliminary test results of the sensor without nanowires demonstrate the process is practical for constructing a nanowire based acoustic sensor, yielding potential benefits for SONAR applications and hearing implants.

DESIGN AND PACKAGING OF AN IRON-GALLIUM (GALFENOL) NANOWIRE ACOUSTIC SENSOR FOR UNDERWATER APPLICATIONS

By

Rupal Jain

Thesis submitted to the Faculty of the Graduate School of the
University of Maryland, College Park, in partial fulfillment
of the requirements for the degree of
Master of Science
2007

Advisory Committee:
Associate Professor F. Patrick McCluskey, Chair/Advisor
Professor Alison B. Flatau, Co-Advisor
Professor Michael Pecht

ACKNOWLEDGEMENTS

I would like to thank my advisor, Dr. Patrick McCluskey, for giving me the opportunity to work on this project, his support and guidance to complete this thesis is highly appreciated. I am also grateful to my co-advisor, Dr. Alison Flatau for her support, direction and mentorship. Her vision and constant encouragement were the biggest motivating factors for this work. I thank the committee member, Dr. Michael Pecht for his time and effort in evaluating my master's thesis work. Thanks to Dr. Keith Herold for giving me the opportunity to start my graduate study at UMD.

I am equally indebted to my research colleague Chaitanya Mudivarthi with whom I spent a lot of time together while carrying out some of the experiments in this thesis. His friendship, support, and technical guidance are greatly valued. Special thanks to my other research colleague, Patrick Downey, who has always been there contributing valuable ideas and helping me understand them. Also, I would like to thank my other colleagues Supratik Datta, Dr. Jin Yoo, Dr. Suok Min Na, Atul Jayasimha for their technical guidance and companionship. All of their feedback and advice has been instrumental in shaping down the work in this project. Also thanks to Matthew James Parsons and Holly Schurter who have recently joined our group for being so nice and supportive.

All my lab buddies at CALCE made it a convivial place to work. In particular, I would like to express my gratitude to Pedro Quintero, Rui Wu, Tim Oberc, Anshul Shrivastava, Lauren Everhart, Leah Pike, Adam McClure, Sony Matthew, Vidyu Challa, Bhanu Sood, for their friendship, support, and numerous contributions in the form of discussions. My

sincere thanks to Dr. Elisabeth Smela and her research group members Mario Uradenta and Marc Dandin for introducing me to MEMS and helping me with the equipments in the cleanroom. I would also like to thank Dr. Ichiro Takeuchi, Jason Hattrick-simpers, Dwight Hunter, Dr. Peng Zhao, Kyu Jang for allowing to use the sputtering machine in their lab and also for helping me in the deposition process and characterization. Special thanks to Tom Loughran, Jonathan Hummel, and John Abrahams for their technical guidance and help in the cleanroom. Their immense patience is greatly appreciated. Also, thanks to Howard Grosenbacher for his help in the machine shop.

I wish to thank my family for their endless love, support and encouragement and taking pride in me and my work. My heartfelt thanks to my sister Richa and her husband Nikhil for their optimism and belief in me and for their constant encouragement through times good and bad. I would like to acknowledge my friend Anurag Tripathi for his continuous support along the way.

Finally, thanks to Ronald Disabatino for sharing the ideas and thoughts with me while starting to work on this project. Thanks to Prof. Beth Stadler and Patrick McGary at University of Minnesota for their collaboration in making nanowires. Last but not the least I would like to acknowledge the support of program officer, Jan F. Lindberg, Office of Naval Research through MURI Grant # N000140610530 and Grant # N000140310954 (ONR 321, Sensors, Sources, & Arrays) for funding this project.

Table of Contents

List of Figures

List of Tables

1. INTRODUCTION

Acoustic sensors are used in a wide variety of applications from hearing aids to sonar to medical imaging to materials characterization. Figure 1.1 shows the potential applications at various frequencies across the acoustic wave spectrum.

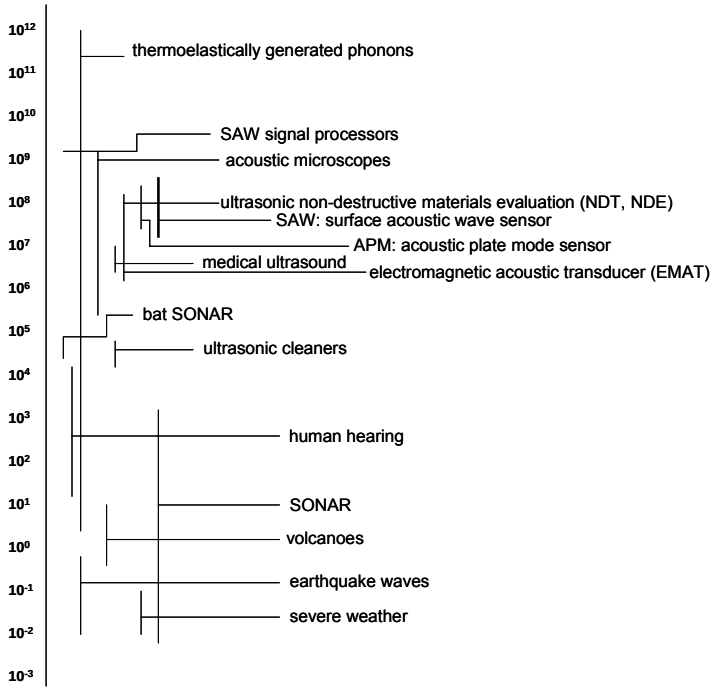

Figure 1.1 Acoustic wave spectrum with specific applications (ordinate shows frequencies in Hz) [1]

1.1. Applications

One of the principle applications of acoustic sensors is SONAR (sound navigation and ranging), which is used to determine the distance and the direction of a remote object by transmitting sound waves and collecting and interpreting the reflected waves (Figure 1.2). SONAR is primarily used for underwater applications. The frequencies used in sonar systems are typically either infrasonic or ultrasonic. To trace objects under water, it is difficult to use alternative methods like LIDAR or RADAR. This is because, in the case of LIDAR, light quickly fades in the water making it difficult to trace underwater objects.

Similarly, RADAR also attenuates in the water and hence can not be used. On the other hand, sound waves travel through water at a speed of 1500 m/s, which is almost five times faster than in air and penetrates to greater depths without deterioration. This makes SONAR a widely used technique for underwater applications.

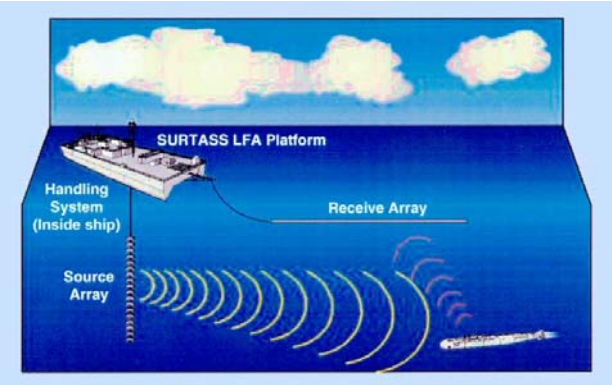

Figure 1.2 Principle of SONAR
(http://www.acsonline.org/issues/sound/illustrations/ill-navySonar.html)

Acoustic wave sensors are also employed to measure film thickness and deposition rate in thin film deposition systems. They are also extensively used to detect defects in materials and changes in material properties due to corrosion or diffusion. They are also commonly used in the field of chemical and biological sensing for both selective and sensitive detection of biochemically active compounds, such as antigens, DNA, RNA, proteins, and bacteria [1]. Also, much research is being done on the implantable acoustic sensors which can emulate the functions of the ear to help millions of people with hearing disabilities [2-4]. For such applications, modern micromachining technology has aided in miniaturizing these sensors. As compared to conventional sensors, MEMS based acoustic sensors are not only sensitive, but they can also be manufactured using batch fabrication techniques at a relatively low cost [5].

The goal of this thesis was to develop a nanowire-based acoustic sensor for underwater applications. The design of the sensor was inspired by the structure, packaging, and transduction mechanism of the human-ear cochlea. The sensor was fabricated using micromachining techniques, incorporating nanowires that mimic stereocilia in the human-ear cochlea [6]. The sensor has been designed to operate primarily for underwater applications.

1.2. Ear: A natural acoustic sensor

The human ear is a broadband acoustic sensor with a wide frequency range (20 Hz – 20 kHz). The human ear as a natural acoustic sensor has an incredible sensitivity in the audible frequency range [7]. It can resolve about 1500 separate pitches with 16,000-20,000 hair cells and can differentiate between sound waves whose frequencies differ by as little as 1 Hz [8]. A brief overview of the human-ear structure and its operation is given in the section 1.2.1. More detailed versions can be found in the literature [9-11].

1.2.1. *Overview of cochlear biomechanics*

Structure: Figure 1.3 is a schematic of the structure of the human ear. The human ear can be divided into three parts: the external ear comprising the pinna and the acoustic meatus. It focuses sound vibrations to the tympanic membrane commonly called the ear drum, at the beginning of the middle ear and aids in determining the location of an acoustic source. The middle ear comprises three tiny bones collectively called auditory ossicles: the malleus, the incus and the innermost bone called the stapes, which is in contact with the oval window of the fluid chamber containing cochlear fluid. Its function is to transform air-born vibrations impinging on the tympanic membrane into acoustic oscillations of the

fluid filling the cochlear duct of the inner ear. In other words, the middle ear bones act as an impedance matching system between the environment and the cochlea. The inner ear consists of two functional units: one is the vestibule and the semicircular canals containing the sensory organs of postural equilibrium and the other is the cochlea, which contains the sensory organ of hearing.

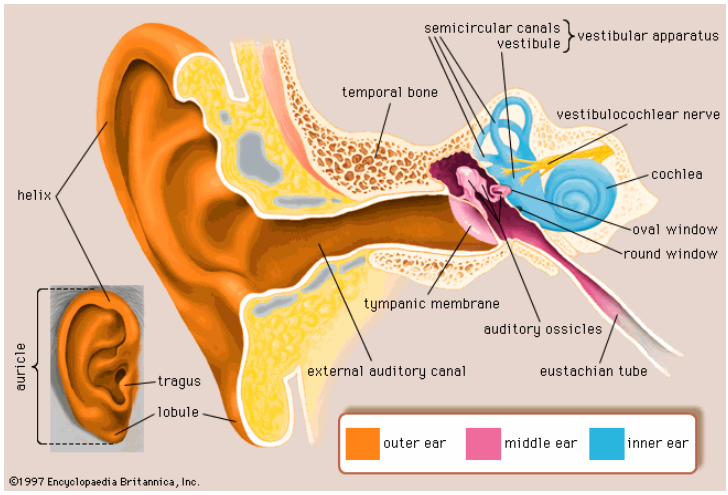

Figure 1.3 Structure of the human ear [9]

Figure 1.4 shows the schematic of the inner structure of the cochlea. The cochlea is a spiral shaped organ consisting mainly of three ducts: scala tympani, scala media (cochlear duct), and scala vestibuli, separated by Reissner's membrane and the basilar membrane respectively. The cochlear duct is filled with endolymph, while the scala vestibuli and the scala tympani are filled with perilymph. They meet each other through an opening at the apex of the cochlea, called the helicotrema. The basilar membrane in the organ of Corti (Figure 1.5) of the cochlea has different acoustic impedances along its length which enable it to spatially resolve different frequencies. While the higher frequency acoustic waves excite the basilar membrane near the base of the cochlea, the lower frequency waves excite it near the apex. The basilar membrane has sensory hair

cells on top of it. Each of these hair cells has hair-like stereocilia projecting from their apical ends. When the stereocilia are deflected under the fixed tectorial membrane due to the motion of the flexible basilar membrane, the hair cells are stimulated, which then send nerve impulses via the vestibulocochlear nerve to the brain stem.

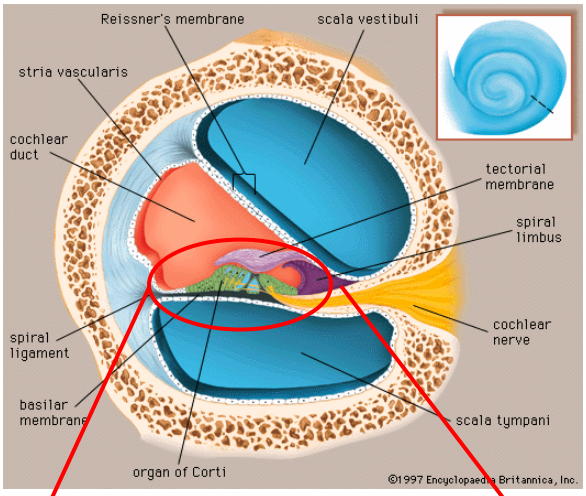

Figure 1.4 Structure of the Cochlea [9]

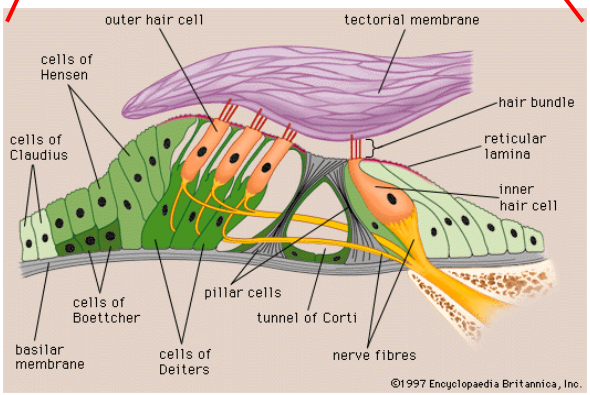

Figure 1.5 Structure of the organ of Corti [9]

Hearing: Figure 1.6 shows the schematic of how sound waves travel from air through the ear and generate nerve impulses responsible for hearing. The acoustic waves enter the outer ear and pass through the external auditory canal to reach the tympanic membrane. This leads the tympanic membrane and the auditory ossicles to vibrate. This results in

stapes motion against the oval window and creates pressure waves in the perilymph of the scala vestibuli of the cochlea. These waves are then transmitted across Reissner's membrane into the endolymph of the cochlear duct. Vibrations in the scala vestibuli also continue to travel around the apex of the cochlea through the helicotrema and transfer the motion into the perilymph of the scala tympani. Higher frequencies do not propagate to the helicotrema but are transmitted through the endolymph in the cochlea duct to the perilymph in the scala tympani. As a result, the basilar membrane vibrates due to the pressure difference across it. This results in an amplified response at a position along its length where the impedance results in a resonant frequency corresponding to the frequency of the incident wave. The motion of the basilar membrane deforms cilia on top of it by shearing them against the fixed tectorial membrane resulting in the stimulation of the hair-cells of the organ of Corti. These hair-cells then fire nerve impulses that travel along the cochlear nerve (a branch of the auditory nerve) to the brain, where they are interpreted as sound. In the meantime, the sound wave in the scala tympani causes the round window to bulge outward and dampen the wave in the perilymph.

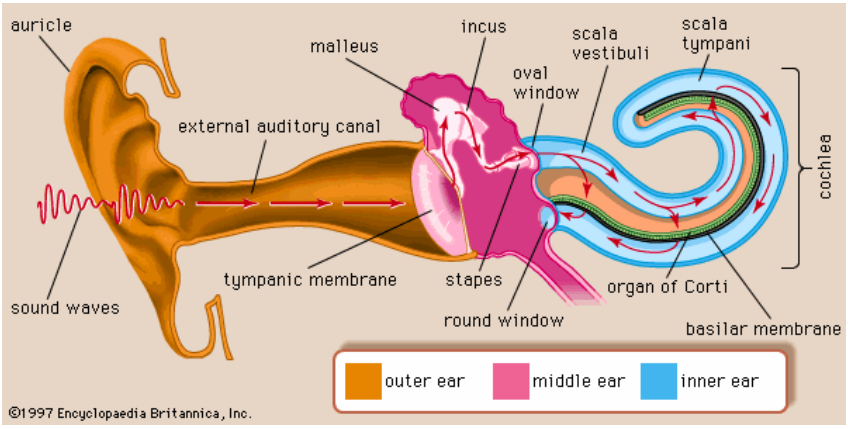

Figure 1.6 The mechanism of hearing [9]

1.3. Different types of acoustic sensors

Many practical devices have been fabricated at the microscale to mimic the cochlear function. Some of them are reported in this thesis as examples. Haronian and Macdonald (1996) [12] proposed an array of silicon beams of gradually varying lengths to mimic the basilar membrane. Their idea was to utilize the silicon beams of different resonant frequencies to mechanically filter the acoustic input into discrete frequency bands and produce corresponding electrical output signals that could be further used for speech recognition, sound localization etc. The beams had a width of 1μm, height of 10 μm, and lengths between 0.37 mm and 7 mm, with resonance frequencies between about 100 Hz and 20 kHz. However, no kind of fluid coupling for transduction of sound waves existed in their structure.

Ando *et al.* (1998) [13] described a fish-bone structure to make an artificial basilar membrane microphone operated in air shown in Figure 1.7. The fishbone structure was formed of 7 μm thick polysilicon beams of different lengths resting on a core backbone of the same material. This backbone was used to transfer vibrations along the device to the lateral beam resonators of individual frequencies, simulating the cochlea's fluid channel function. However, the input transverse beam unlike cochlear fluid was too stiff to vibrate properly to the acoustic input signal.

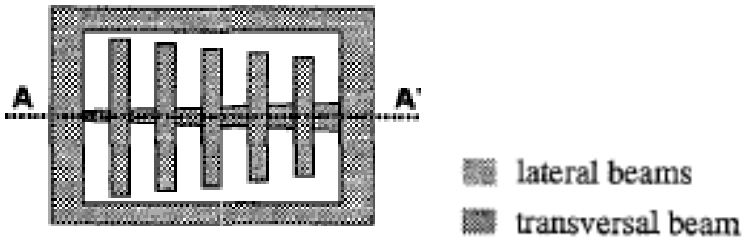

Figure 1.7 Silicon micro-fishbone structure as artificial basilar membrane microphone [13]

Hemmert et al. (2003) [14] proposed a two duct fluid-filled MEMS-based mechanical cochlea. A 3.5 cm long, 1-3 μm thick, and 1-2 mm wide membrane similar to the basilar membrane was built using SU-8 polymer. Filtered water was used as the filler fluid. The authors used the impulse response at two very closely spaced locations to demonstrate the existence of a traveling wave and demonstrated up to 30π phase accumulation.

White and Grosh (2005) [15] reported on another two duct fluid filled MEMS cochlea design with a tapered basilar membrane made of silicon nitride beams embedded in a polymer. Silicon nitride was used for beams to reduce the residual stress in them. The width of the beam array varied between 10 and 20 μm with beams spaced 2 to 4 μm apart. The membrane had 32 capacitors spaced along its length to get the vibration of individual beams in response to the different frequencies of sound ranging from 100 Hz to 10 kHz.

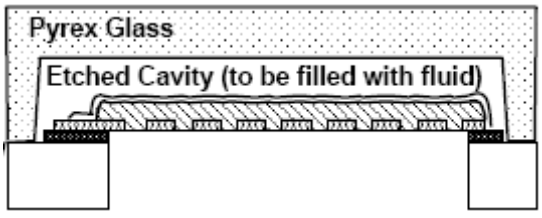

Figure 1.8 Cross-sectional view of the device without the fluid [15]

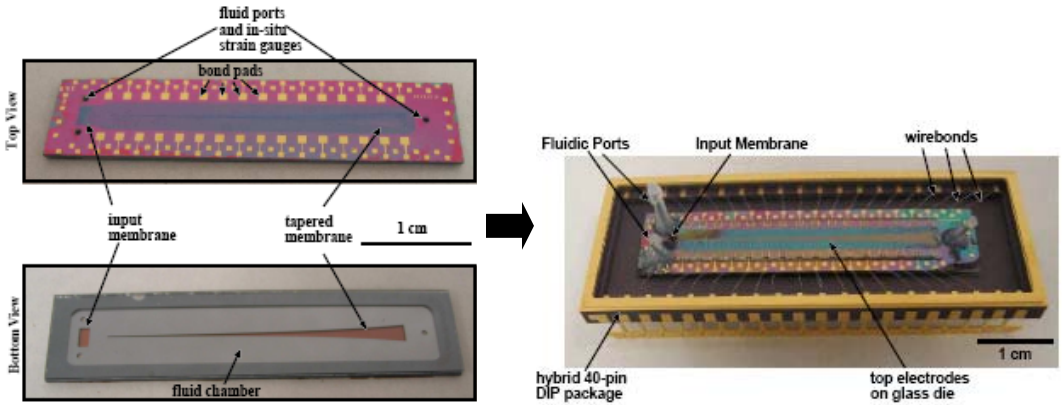

Figure 1.9 Picture of the final device with the top electrode die bonded and wirebonded into a package. This device had been filled with silicone oil [15]

A few examples of micromachined microphones as well as hydrophones in the literature are also listed here. These sensors are not biologically inspired and emphasis is paid to the sensing mechanism and fabrication approach. Scheeper et al. (1993) [16] designed and fabricated a microphone, which could operate up to the frequency of 20 kHz. Figure 1.10 shows the cross-sectional view of the microphone. The microphone consisted of two wafers: a diaphragm and a backplate wafer joined together by gold-gold thermocompression bonding. The diaphragm wafer consisted of a 1.95 mm diameter and 0.5 μm thick silicon nitride membrane coated with gold electrodes and the backplate wafer consisted of the gold circuitry for capacitive sensing. The microphone required an external power supply, since it was a condenser microphone. The sensitivity approached -33 dB re 1 V/Pa for this microphone.

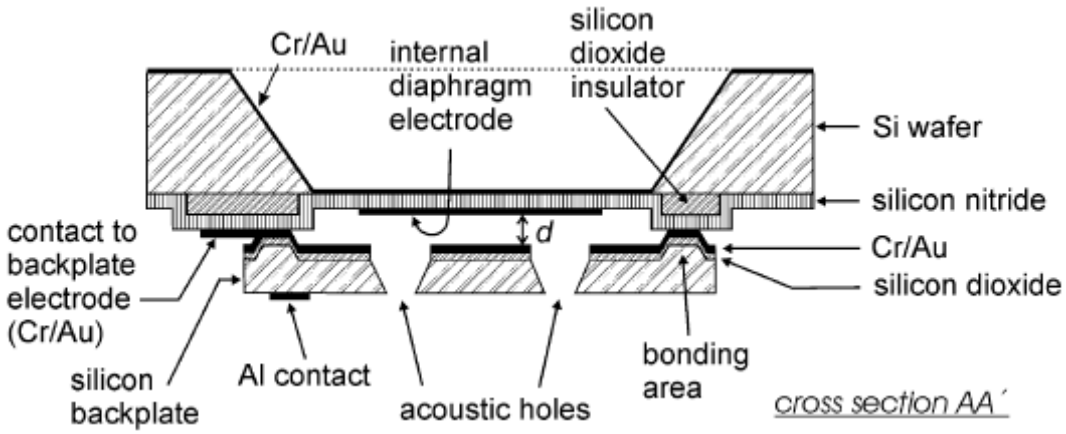

Figure 1.10 Cross-sectional view of the silicon nitride microphone by Scheeper et al. [16]

Bernstein et al. (1997) [17] fabricated a ferroelectric sonar transducer utilizing a MEMS sol-gel PZT array to measure the vibration of a silicon membrane. The device (Figure 1.11) consisted of 8x8 arrays and was operated in water in the frequency range of 0.3 to 2 MHz. A 10 μm silicon membrane was formed by an anisotropic wet etching process using EDP, on top of which PZT was patterned. The authors reported sensitivity of the device reaching -235 dB *re* 1 V/μPa.

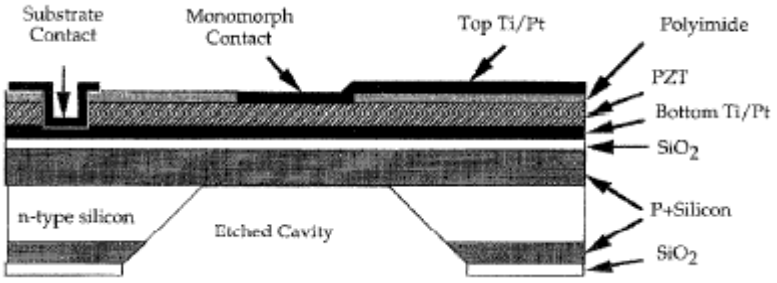

Figure 1.11 Cross-sectional view of the PZT hydrophone [17]

1.4. Proposed sensor

As discussed earlier in section 1.3, it can be observed that a majority of existing acoustic sensors, including cochlear-like sensors, are based on membrane deflection to detect sound. However, typically in cochlea, both basilar and tectorial membranes are needed to convert acoustic waves into mechanical stresses in stereocilia. Stresses in the cilia arise as a result of their shearing against the more rigid tectorial membrane when the basilar membrane deflects in response to acoustic pressure oscillation. It is the shearing of these stereocilia that ultimately triggers biochemical reactions that cause hair-cells to send nerve impulses to brain. Figure 1.12 (left) shows the hair-like stereocilia present in human-ear cochlea.

Also, cilia play an important role in the hearing mechanism of fish and other aquatic animals. In fish, instead of a cochlea, they have a lateral line, a sense organ which helps the fish to avoid collisions, locate prey, and orient itself in relation to water currents. The lateral line is a collection of small mechanical receptors composed of a group of hair cells called neuromasts located under the skin in fluid-filled canals on the body of all fish [18]. The hair cells are the same sensory cells found in the human-ear cochlea. The ciliary bundles when stimulated by the sound waves activate the hair cells to transduce mechanical energy into electrical energy. The electrical signals are carried to the brain through nerves, which allows fish to perceive sound similar to the principle of hearing in the human ear. Figure 1.12 (right) shows the cilia bundles from a lizard fish.

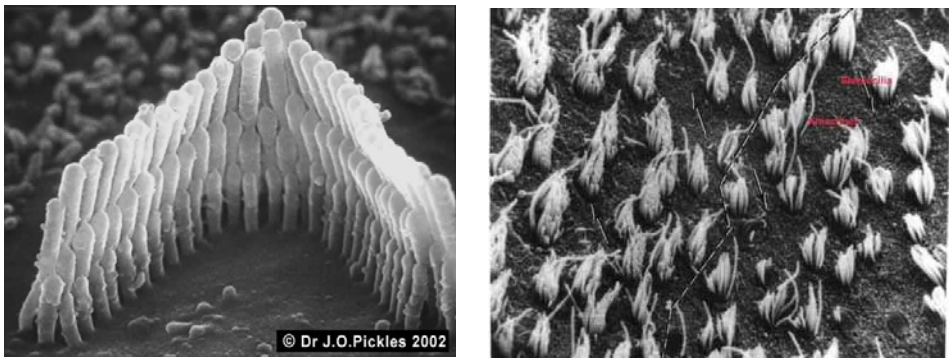

Figure 1.12 Human-ear stereocilia [19] (left), cilia bundles from a lizard fish [20] (right)

Therefore, using artificial cilia made of magnetostrictively active material, it is possible to emulate the function of stereocilia. Magnetostrictive materials are active materials that respond to mechanical forces by changing their magnetization. A brief introduction to the use of magnetostriction and magnetostrictive materials as sensing elements is given in the next section. The biological stereocilia have diameters of the order of tens of nanometers and a large aspect ratio. The technological difficulty of making nanowires out of active materials at scales comparable to the nanoscale stereocilia geometries has precluded the imitation of stereocilia. However, recently Stadler et al. at Minnesota (2006) [6] have succeeded in fabricating FeGa alloy nanowires, which are magnetostrictive in nature (shown in Figure 1.13). If the dimensions of these nanowires are orders of magnitude smaller than that of the membrane, they can be extremely sensitive to small strains. The nanowires grown are small in dimension (~100 nm dia and 80 μm long) and are grown in close-packed arrays similar to cilia. This enables the possibility of making an acoustic sensor with high sensitivity and high bandwidth in a small area similar to the human cochlea [8].

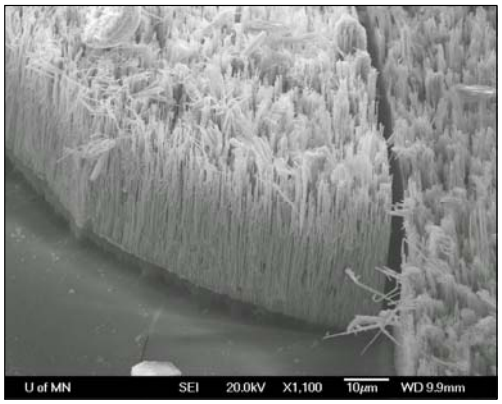

Figure 1.13 FeGa (Galfenol) nanowires

The proposed nanowire acoustic sensor was motivated by the architecture of the human-ear cochlea. It is a micromachined device consisting of an elongated cavity with two fluid channels and a flexible membrane partition between them, playing the role of the basilar membrane. The nanowires made of FeGa are to be attached to this flexible membrane on one side and in contact with the fixed membrane on the other side. As described above, the nanowires are used to mimic the functionality of the stereocilia and the fixed membrane is used to emulate the tectorial membrane. The nanowires respond to the external forces by changing their magnetization, and a magnetic sensor is used to measure these changes.

Fabrication was the major challenge associated with building this cochlear-like sensor. Since it is a microscale device, micromachining techniques were employed. Since the sensor has been primarily designed for underwater applications, its packaging is also more challenging than that of microelectromechanical devices used in ambient environments. The inspiration for the external package design of the sensor was also derived from the structure and the transduction mechanism of the cochlea and the

structure of the hearing organ of the fish. The tissues composing the body of the fish have the same acoustic impedance as that of the water. This allows sound to pass through them with minimum attenuation and interact with the lateral line in which the ciliary bundles (analogous to cilia on hair cells in the basilar membrane in the cochlea) are found inside the fish body [21]. In the human ear, middle ear bones ensure impedance match between the low impedance acoustic oscillations in the tympanic membrane and the high impedance fluid in the cochlear duct. Inspired from them, the package was designed to include an acoustically transparent window minimizing the attenuation of sound passing through it. For this, the material and fluid medium must be selected such that their acoustic impedance matches closely to that of sea water in order to minimize the reflection of incoming sound waves at material interfaces. For this purpose, the acoustic performance of different package materials filled with fluids has been investigated. These studies were conducted in water and quantified package and fluid impedance and attenuation characteristics and moisture absorption properties.

1.5. Background on Magnetostriction

Magnetostrictive materials are a special subset of ferromagnetic materials, which can be broadly defined as materials that undergo a change in physical dimensions when subjected to a magnetic field and conversely, undergo a change in their magnetization when subjected to an externally applied stress. The effect was first identified in 1842 by James Joule. The internal crystal structure of the magnetostrictive material is divided into domains, each of which is a region of uniform magnetic polarization. In the absence of a magnetic field or stress, the series of domains have randomly oriented magnetic moments. When a magnetic field is applied, the boundaries between the domains (domain walls)

shift, rotating the domain. Due to the realignment of magnetic domains in the direction of the field, there is a change in the material's length Δl called magnetostriction, and a change in the magnetic induction B of the sample. Magnetostrictive materials induce strain irrespective of the polarity of applied magnetic field. This is known as Joule's effect and is used for actuation purposes.

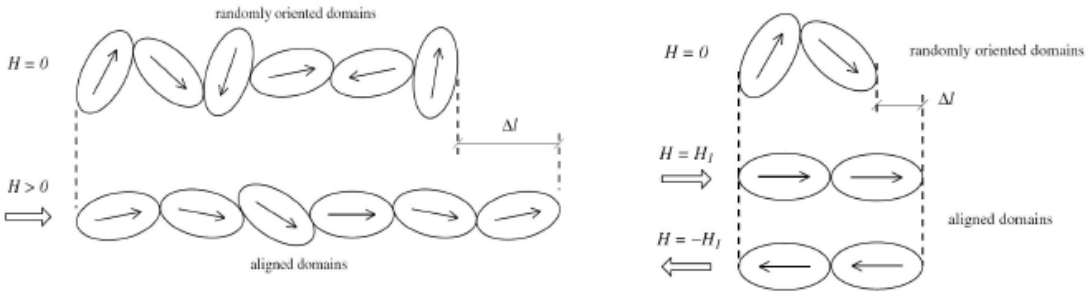

Figure 1.14 The rotation and movement of magnetic domains causes a physical length change in the material (Joule's effect). (b) Independence of strain on polarity of applied field [22].

It is a common practice to apply compressive pre-stress on the magnetostrictive material if used for actuation purposes, which can be easily explained using Figure 1.15. When there is a maximum compressive pre-stress applied, the domains become normal to the direction of the applied stress and as the field is increased, these domains realign parallel to the direction of the applied stress and thus maximum magnetostriction, λ_{max} can be achieved. Figure 1.16 shows a set of magnetostriction versus magnetic field curves (or λ-H curves) at various levels of mechanical pre-stress. The corresponding positions A, B, and C from Figure 1.15 can be seen on the graph in Figure 1.16. Point C indicates the saturation state.

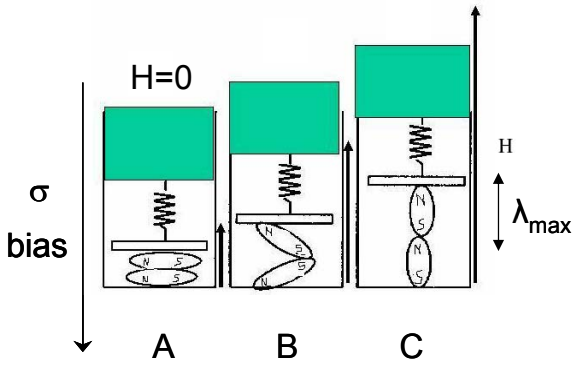

Figure 1.15 Schematic illustrating actuation behavior in magnetostrictive materials (Joule's effect) with the help of rotation of magnets [23]

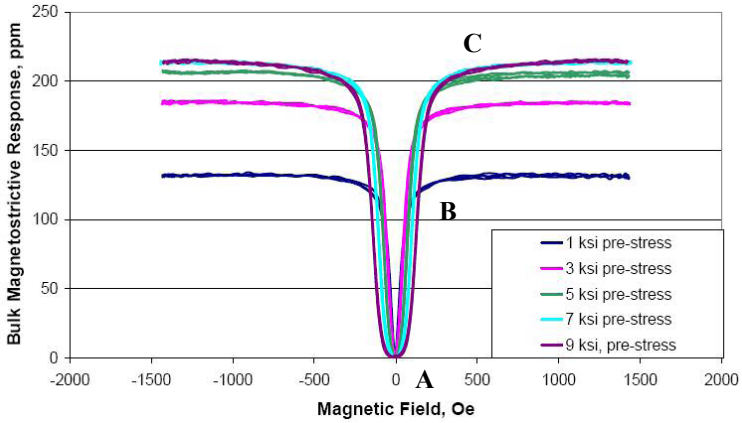

Figure 1.16 Actuator characterization curves of Magnetostriction vs Magnetic field for 18.4% gallium Galfenol for various stress levels [22]

Conversely, the magnetic flux density of the material changes when subjected to a mechanical stress. This is called the Villari effect. The Villari effect is used for sensing applications. A biased magnetic field is usually applied to the magnetostrictive material to maximize the change in the magnetic flux density ΔB in response to a given stress application. This is because the bias field aligns the domains parallel to the direction of the field resulting in a net magnetization along that direction. When a compressive stress is applied, the domains re-orient, changing the net magnetization resulting in magnetic flux density change, ΔB. This is illustrated in Figure 1.17 and Figure 1.18 . It should be

noted that in the absence of a biased magnetic field there will not be any initial magnetization and hence the resulting change in the magnetic flux density due to the application of stress will be zero.

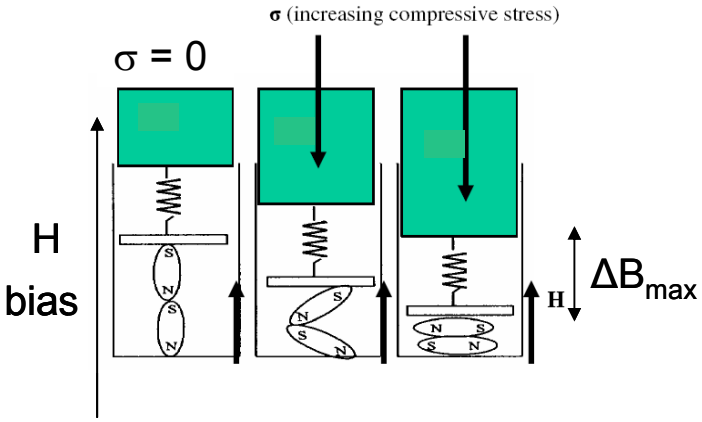

Figure 1.17 Schematic illustrating sensing behavior in magnetostrictive materials with the help of rotation of magnets. The stress applied to a magnetostrictive material changes its magnetic flux density (Villari effect) [23]

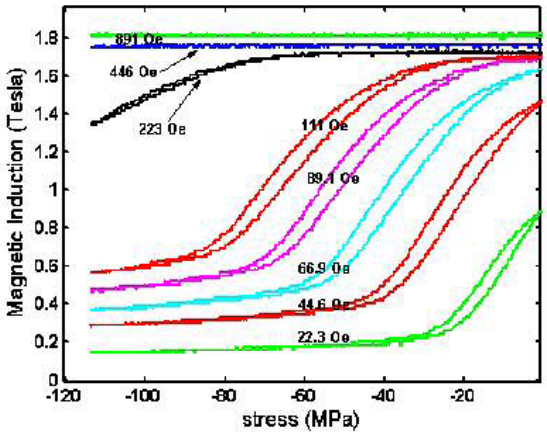

Figure 1.18 Magneto-mechanical sensor characterization curves of a 19% gallium Galfenol [24]

The most common unit systems to define magnetic quantities are either Gaussian /CGS system or SI system. The table below shows the units and conversion factors for common magnetic quantities for reference purposes.

Table 1-1 Unit system and conversion factors for magnetic quantities

Quantity	CGS units	Conversion factor CGS ---> SI	SI units
Magnetic field strength (H)	Oersted (Oe)	79.58	A/m
Magnetic flux density (B)	Gauss (G)	1×10^{-4}	Tesla (T)
Magnetization (M)	emu/cc	1×10^{3}	A/m
Magnetic flux (φ)	Maxwell (Mx)	1×10^{-8}	Weber (Wb)
Magnetic permeability (μ)	Dimensionless	$4\pi \times 10^{-7}$	H/m

1.5.1. **Magnetostrictive materials**

Nickel and iron are the materials in which magnetostriction was first observed (45 ppm for nickel, 15 ppm for iron) [22]. Since then, alloys of iron have been discovered that exhibit a "giant" magnetostrictive effect under relatively small fields. Terfenol-D, a specially formulated alloy of Terbium, Dysprosium, and Iron is a very popular giant magnetostrictive material that exhibits a large magnetostriction of 2000 ppm in a field of 2 kOe at room temperature. However, it is brittle, with an ultimate tensile strength of 28 MPa, limiting its application only to uniaxial stresses [25]. Therefore, other alternative materials are being investigated, which not only show high magnetostriction but are ductile and machinable.

Galfenol

One magnetostrictive material under current investigation is an iron-gallium alloy ($Fe_{1-x}Ga_x$) termed Galfenol which appears to be a promising material for a variety of actuator and sensing applications. It exhibits magnetostriction peaks (~350-400 ppm) at 19 and 27 atomic % gallium at low applied magnetic fields (~100 Oe) and has very low hysteresis [26]. Figure 1.19 shows saturation magnetostriction values measured for different stoichiometries of single crystal Galfenol with 10 to 35 atomic % gallium content. In

addition to these unique magnetostrictive properties, Galfenol has good mechanical properties and can be machined. Galfenol's elastic modulus, permeability, and piezomagnetic coefficients are quite constant over temperatures ranging from -20°C to +80°C [26] and it demonstrates high tensile strength (~500 MPa), good machinability, and good ductility [27, 28]. In addition to the transduction properties of Fe-Ga alloys, their ability to withstand shock loads and harsh operating environments, and to operate in both tension and compression, and hence in bending, makes them suitable for a variety of sensors and actuators including those at the micro and nanoscales [29].

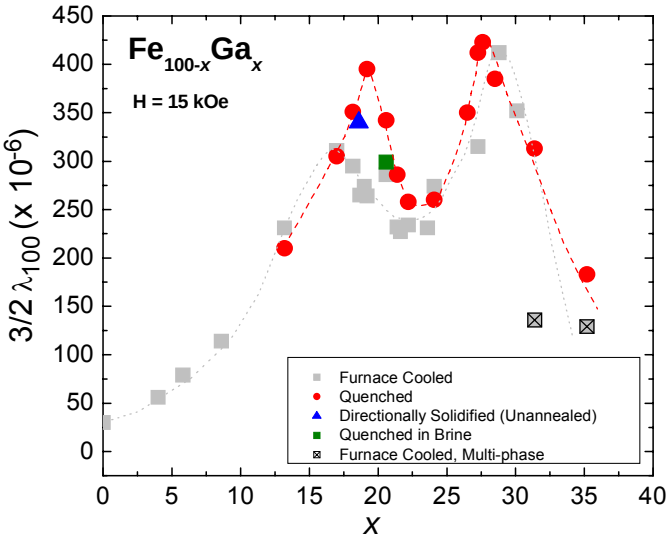

Figure 1.19 Magnetostriction versus Gallium content in single crystal Galfenol [26]

Magnetostrictive materials are often used as transducers in acoustic underwater systems for geophysical surveying and exploration, ocean tomography, mine clearance, underwater information exchange, and underwater sonar systems. They are also used as broadband vibration sources in speakers, as well as in laboratory and industrial shakers. Ultrasonic, high-frequency, high-power magnetostrictive actuators are used in medical, dental, petrochemical, and sonochemical applications [22]. Sensor systems, such as force,

moment and torque meters, based on magnetostrictive transduction are also under use [23].

Both piezo-electric and magnetostrictive materials demonstrate very high bandwidth (~100 KHz) making them well suited to high frequency applications such as vibration control and SONAR. However, piezo-electric materials require very large electric fields (~5 kV/cm) and may suffer from self-heating problems. On the contrary, magnetostrictive FeGa alloys posseses some promising properties, such as high tensile strength (20 times that of typical piezo-electric), lower bias field for actuation, and the ability to withstand underwater shocks and explosions. These characteristics may enable the use of these alloys as compact actuators and sensors in harsh and shock prone environments. In addition, the ability to use small permanent magnets with low hysteresis limits self-heating, making them potentially better choices for these applications than piezo-electrics. This is also a direct application of magnetostrictive actuation without any necessity for stroke amplification and has been very popular with the Navy [23].

1.5.2. **Nanowire Fabrication**

As discussed in section 1.4, Galfenol nanowires in an acoustic sensor mimic the action of hair-like stereocilia present in human ear and other biological species [6]. Since bending of these naowires results in simultaneous compression and tension, the net magnetization change in the nanowire would average to zero if the alloy was uniformly isotropic and the trends in magnetization change due to tension and compression were similar. However, the change in the magnetization of a FeGa alloy in compression is significantly larger than in tension. Therefore, during bending, the response of the galfenol nanowire is

dominated by the compression. This has been demonstrated at the bulk level by Downey et al. [29]. Hence, FeGa nanowires are ideal for artificial cilia applications. Their other potential applications are in fluid flow sensing and detection of chemical contamination [30].

The Galfenol nanowires being grown at the University of Minnesota are 20-200 nm in diameter and about 25-100 μm in length. Figure 1.20 shows the nanowire fabrication process [30-32]. The fabrication procedure for making nanowires starts with electropolishing and first anodization of aluminum, thus creating a porous template. These pores are not straight and uniform and hence this disordered alumina is etched away with 1.8 wt% chromic and 6 wt% phosphoric acid for 20 min, leaving small dimples at the aluminum surface. A second anodization is done which creates ordered pores with uniform diameters and spacing. The remaining aluminum is etched away from the back side along with the barrier layer with saturated $HgCl_2$ (mercuric chloride) solution leaving straight through holes in the template. A copper electrode is then sputtered on the back of the template and FeGa alloy is electrochemically deposited into the pores. Later, the alumina template is etched back exposing the nanowires.

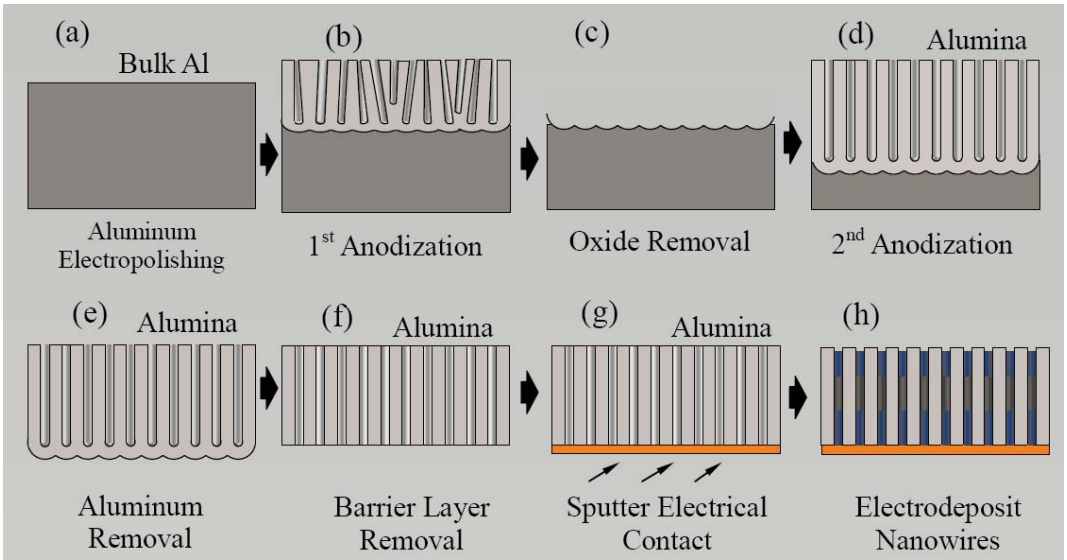

Figure 1.20 The nanowire fabrication process [30]

As discussed in section 1.5, it is important to bias FeGa to use it as a sensor. For this purpose, research is underway to grow the nanowires with an initial cobalt layer that can act as a bias layer. Also, as discussed in section 1.4, a magnetic sensor must be used to measure the change in the magnetization of these nanowires in response to the motion of the flexible membrane. However, even the smallest sensing area of a commercially available magnetic sensor (~ 50 μm x 50 μm for GMR – giant magnetoresistive sensor made by NVE Volatile Inc.) is significantly larger than the nanowire diameter. Also, the whole GMR sensor is about 4.5 mm x 3 mm in size, which makes it extremely difficult to use with the micromachined nanowire acoustic sensor. Therefore, attempts to grow nanowires with the magnetic bias layer (Co), active layer (FeGa) and GMR layer (Cu/Co) all integrated are underway to completely eliminate the need for a commercial GMR sensor [33]. With the GMR sensor integrated within the nanowire, it would be possible to measure the response of each individual nanowire. However, in the work presented in this thesis, the sensor was designed to be used with a commercial GMR sensor.

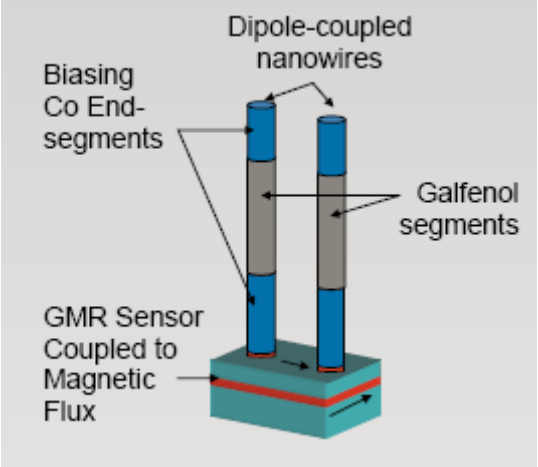

Figure 1.21 Nanowires coupled with Co bias layer and multi-layered GMR sensor [30]

1.6. Organization of this thesis

The organization of this thesis and contributions towards the design, fabrication, and preliminary testing of the iron-gallium nanowire based acoustic sensor is summarized below:

Chapter 2: **DESIGN –** ***Analogy to Human-Ear Cochlea***

This chapter discusses the iron-gallium nanowire acoustic sensor structure and operation as an analogy to the human-ear cochlea. It includes the challenges related to the identification of the key components of the sensor and their respective material selection. There are three main components responsible for the effective operation of the sensor – magnetic flux path, membrane structures (playing the role of the basilar and tectorial membrane), and external packaging. Packaging plays an important role as the sensor is mainly meant for use in underwater applications.

Chapter 3: **Process Sequence for Fabricating the Sensor**

The micromachining processes and techniques and the process sequence used for the fabrication of the nanowire based acoustic sensor are discussed in detail. This chapter also includes the limitations and challenges encountered while using these micromachining techniques for the fabrication of such a miniaturized sensor. Design efforts and solutions for developing this acoustic transducer have been described in this chapter.

Chapter 4: **Experimental Testing**

This chapter focuses on the test setup and procedure for testing the three key components of the sensor. The first set of experiments tested the response of the device membrane in air using a Laser Vibrometer. The second experiment involved qualitative magnetic force microscopy (MFM) testing of a nickel thin film used as a magnetic flux path. The third experiment was the acoustic testing of the candidate encapsulants and filler fluids. Lastly, an experiment was performed to test the response of the packaged device in water. The preliminary testing of the device was done without nanowires as they were not available at that time. The chapter includes the results and inferences obtained from those experiments and also discusses the limitations in the measurement techniques and equipment.

Chapter 5: **Conclusions and Contributions**

This chapter summarizes the steps involved in the development of the nanowire based acoustic sensor and the significant contributions made in the work.

2. DESIGN – *ANALOGY TO HUMAN-EAR COCHLEA*

Many aspects of the transduction mechanism, design, and packaging of the iron-gallium nanowire acoustic sensor are analogous to (and are inspired from) those found in the human-ear cochlea. Figure 2.1 and Figure 2.2 are drawings of the cross-sectional view of an uncurled human-ear cochlea and the iron-gallium nanowire acoustic sensor, respectively. The figures indicate the analogy between the biological human-ear cochlea and its mechanical counterpart – the nanowire acoustic sensor. It can be observed that in the cochlea there are two fluid channels separated by the basilar membrane. The oval window and the round window are flexible membranes at one end of the upper and lower channels, respectively. The oval window facilitates transfer of acoustic pressure oscillating into the cochlea. The round window facilitates pressure equalization and helps damp out acoustic oscillations in the chamber. Connecting these two channels is helicotrema which allows the sound waves to travel from the top to the bottom channel thereby doubling the pressure difference across the basilar membrane and hence amplifying its motion. Analogous to this, the nanowire acoustic sensor consists of two fluid channels with a window on one side of both the channels. While the acoustically transparent window that allows sound waves to reach the sensor is analogous to the oval window, the other window that damps the sound waves is analogous to the round window. An opening on the other side, connecting the two channels, is similar to the helicotrema. There are two membranes in the cochlea. The one separating the two channels is the basilar membrane, which moves in response to the sound waves and has stereocilia on top of it. The other one is the fixed tectorial membrane against which stereocilia shear when the basilar membrane moves/vibrates. The flexible and fixed membranes in the

mechanical sensor play the roles of basilar and tectorial membranes respectively. The nanowires (often referred to as artificial cilia) in the mechanical sensor not only dimensionally but also functionally mimic the stereocilia.

A difference in impedances (or impedance mismatch) of two media results in the reduced sound transmission. The tympanic membrane and the ossicles in the middle ear function to overcome the mismatch of impedances between air and the cochlear fluids and thus reduce the resistance to the sound passage. Similarly, the challenge involved in the nanowire acoustic sensor is to minimize the difference in impedance between sea water and filler fluid thus minimizing the transmission loss before the sound reaches the sensing element. The use of acoustically transparent materials and filler fluids in the sensor allows the sound waves to pass with little attenuation. Mechanical amplification as is accomplished in the middle ear is not addressed in the current design considerations, but is encouraged as a consideration for future impedance matching concepts.

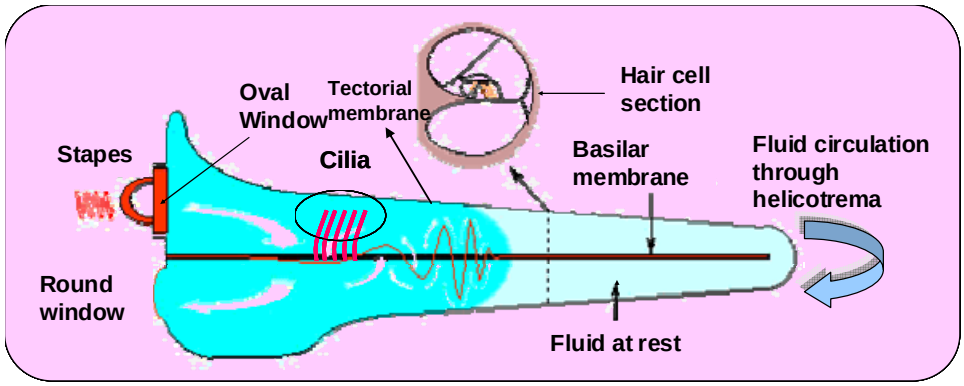

Figure 2.1 Schematic of the cross-section of the human-ear cochlea (http://www.vimm.it/cochlea/cochleapages/theory/hydro/hydro.htm)

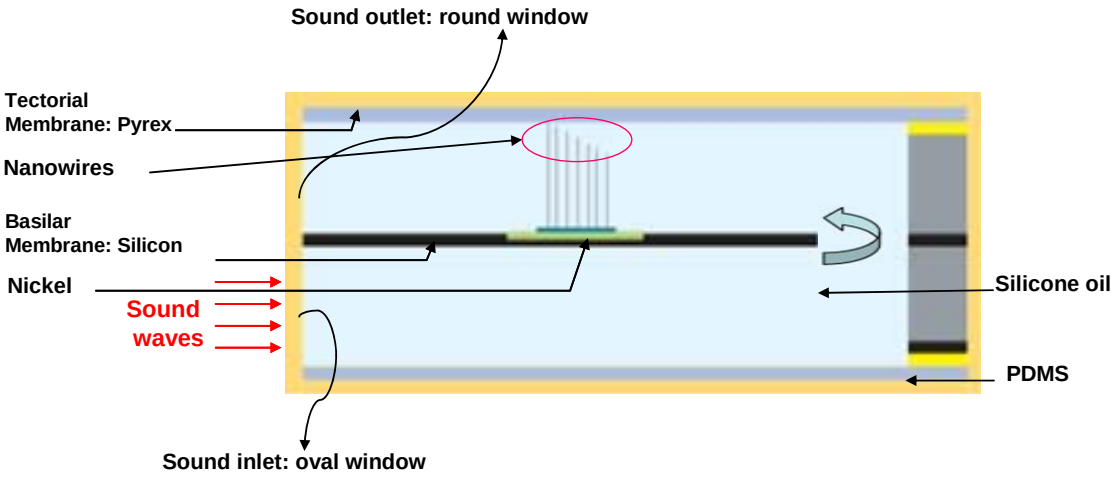

(a)

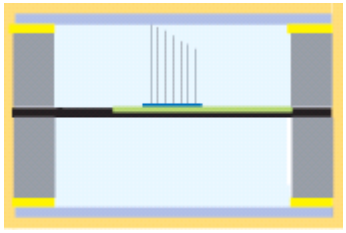

(b)

Figure 2.2 Schematic of the (a) front, (b) side cross-section of the iron-gallium nanowire acoustic sensor

Based on the physiology and transduction process of the human-ear cochlea, the acoustic sensor includes a fluid cavity corresponding to the fluid-filled cochlea. The cavity consists of a flexible membrane similar to the basilar membrane in the cochlea, which vibrates in response to sound waves. At the top of the flexible membrane, Galfenol nanowires analogous to stereocilia are attached. Another membrane fixed in nature and functionally similar to the tectorial membrane lies above and touches the free end of the Galfenol nanowires. On interaction with the sound waves, fluid in the cochlea sets in motion and vibrates the basilar membrane, shearing cilia against the tectorial membrane. The sheared cilia trigger the hair-cells to fire an electrical signal. Similarly, in the

acoustic sensor, the flexible membrane vibrates because of fluid action in response to sound waves, displacing the nanowires and shearing them against the fixed membrane. The bending of the magnetostrictive nanowires causes a stress induced change in the magnetic flux density that could be measured by a magnetic sensor that provides a corresponding electrical output. It should be noted that there is a difference in the sensing mechanisms of the ear and the mechanical sensor. Electrochemical reactions triggered in the hair cells by the moving cilia generate nerve impulses in the ear. However, in the proposed mechanical device, a magnetic sensor gives a voltage output proportional to the stress induced change in the magnetic flux density of the nanowires.

2.1. Design and Operation

Device Structure

The iron-gallium nanowire acoustic sensor is a MEMS scale and a bio-inspired sensor that is analogous to the human-ear cochlea. The manufacturing and packaging of the acoustic sensor is done using micromachining techniques at the wafer level, which is not only cost-effective but also allows fragile, contamination-sensitive nanowires to be protected in the ultra-clean environment of the fab. Figure 2.3 and Figure 2.4 show the three-dimensional view of the cochlea and the acoustic sensor, respectively.

The nanowire acoustic sensor consists of a square flexible membrane of silicon fabricated with the help of photolithographic techniques on top of which is attached the nanowire substrate. The dimensions of the membrane were chosen from 1 mm x 1 mm to 3 mm x 3 mm depending on the size of the substrate of nanowires available from Prof. Stadler at

the University of Minnesota. The membrane is fixed from two sides and separates the fluid cavity into two parts similar to the basilar membrane as explained in the previous section. Use of a low viscosity liquid medium inside the package was preferred in order to reduce viscous damping of the nanowire motion. The liquid also transports the acoustic pressure waves coming from the oval window (acoustically transparent window) to the flexible membrane and hence it must be close in acoustic impedance to the window material and the sea water to minimize sound reflection. The channel below the membrane has two open ends; one of them is encapsulated with an acoustic impedance matching material to allow the sound waves to enter through the package with minimal attenuation. These sound waves interact with the impedance matched fluid inside the channels to vibrate the membrane. The other end of the bottom channel connects to the top channel allowing the flow of sound waves through the fluid. This results in effectively doubling the pressure difference across the membrane, which results in its greater displacement. One of the ends of the top channel acts similar to the round window in the cochlea damping out the sound waves without creating any reflections and echoes within the sensor cavity. For this purpose, the window must be filled with a material of low impedance compared to the fluid in the chamber. This can be ensured by introducing air pockets in the encapsulation material, which will diffuse the acoustic oscillations. However, in the current design use of such low impedance material has not been addressed. Nevertheless its use in future designs is recommended. The nanowires were glued on the flexible membrane with a thin film of photoresist (SU-8). It is difficult to estimate the thickness of this film of photoresist, which is one of the reasons why it is encouraged that nanowires be grown directly on nanowires is encouraged to be

integrated with the membrane surface in the future design. A fixed membrane (similar to the tectorial membrane) of either pyrex or silicon is bonded along with the flexible membrane to a spacer silicon wafer of thickness equal to the length of the nanowires. This will ensure the nanowires attached to the flexible membrane are in contact with the fixed membrane at their free end. This is important because it is the bending or shearing of these nanowires as a result of the wiggling of the flexible membrane in response to the sound waves that results in a change in the magnetic flux density. The bonding between the two membranes was achieved by cold welding of pure indium solder at room temperature creating a hermetic joint.

A commercially available GMR sensor attached to the acoustic sensor measures the change in the magnetic field due to the bending of nanowires and gives an electrical output. However, the GMR sensor available was 15 mm x 4 mm in dimension and therefore, could not be placed in the same fluid cavity as the nanowires. A preliminary finite element model of the nanowires done by Mudivarthi [34] showed that the GMR sensor should be placed as close to the nanowires as possible to detect the minute changes in magnetic flux density resulting from their pressure induced bending. To permit the GMR sensor to be remotely located while still receiving detectable levels of magnetic flux density required the deposition of a thin film of material with good magnetic properties to serve as a closed magnetic flux path between the nanowires and the GMR sensor. The pressure induced bending of nanowires results in magnetic state changes which are carried along a flux path to the GMR sensor without significant losses. Ongoing research to integrate the GMR sensor with the base of the iron-gallium

nanowires is being conducted by Prof. Stadler at University of Minnesota as discussed in section 1.5.2. This would eliminate the use of the large commercially available GMR sensor and thus help in further miniaturizing the sensor.

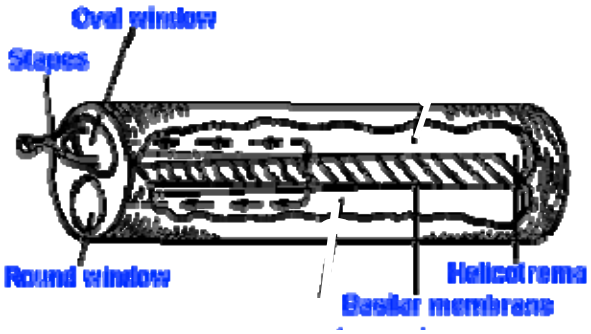

Figure 2.3 Representation of the 3-D view of uncoiled biological cochlea [35]

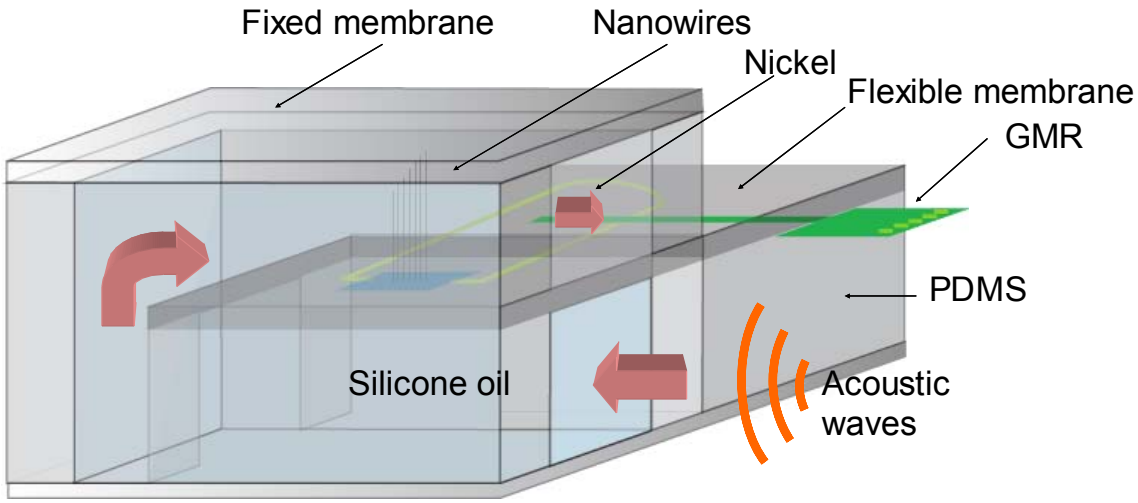

Figure 2.4 Schematic of a 3-D view of the Galfenol nanowire acoustic sensor

Device Operation

A description of the operation of the device (i.e. how acoustic waves in the ambient underwater environment are converted to electrical signals by the device) is presented next. When an acoustic pressure wave impinges on the acoustically transparent window, part of the wave is reflected and the remaining part is transmitted through the window to

the filler liquid inside the sensor. The fraction of the reflected or transmitted acoustic waves depends on how well matched the impedances of the encapsulation material and the filler fluid are to the sea water. The closer the impedance of the window and fluid are to the impedance of sea water, the more acoustically transparent they are to the pressure wave. The encapsulation material and filler fluid were chosen to maximize energy transmission to the filler fluid.

As a result of the incoming acoustic waves, the flexible membrane in contact with the fluid begins to vibrate. The fluid medium inside the closed cavity can result in additional impedance when it cannot move freely during the vibration. The opening provided at the end of the channel helps to alleviate this problem by maintaining pressure balance at both sides of the vibrating membrane similar to helicotrema in the cochlea. In addition, it helps in doubling the pressure difference across the flexible membrane for greater displacement of the membrane. Due to this displacement of the flexible membrane, fine nanowires that are cantilevered normal to the plane of the membrane get sheared back and forth relative to where the opposite end of the nanowire is pressed against the fixed membrane. The shearing stress induces change in the magnetic flux density proportional to the bending of these magnetostrictive iron-gallium nanowires. A magnetic flux path connects the flux lines from the nanowires to where they can be sensed by a commercially available GMR sensor to give an electrical voltage output that is proportional to the original acoustic pressure wave.

2.1.1. **Key components of the sensor**

The structural design of the nanowire acoustic sensor consists of three important components, which are critical for effective operation. Proper material selection and testing for all the components is essential before they can be incorporated in the sensor. This is explained in detail in sections 2.1.1.1- 2.1.1.3.

2.1.1.1. Flexible and fixed membrane: Basilar and Tectorial membrane

The flexible membrane in the sensor is functionally similar to the basilar membrane. It is square shaped, supported on two sides and vibrates as a result of interaction with the sound waves. The purpose of the flexible membrane is to amplify the vibration of the nanowires in response to the acoustic waves by virtue of its greater surface area. Early FEA predictions of the vibration of Galfenol nanowires immersed in a fluid medium [34], indicated that nanowires attached to a rigid surface would not respond sufficiently to the acoustic waves to produce a measurable change in the magnetic flux density. Being nanoscale in dimension, the pressure difference across these nanowires is too small to deflect them appreciably. When these nanowires are attached to a membrane of greater surface area, the higher force on the membrane surface leads to its larger deflection. The larger deflection of the flexible membrane leads to the larger shearing of the nanowires under the fixed membrane, consequently producing greater change in the magnetic flux density.

2.1.1.1.1. Material selection

The membrane is a critical part of the nanowire acoustic sensor. It should not only be flexible but also be able to withstand the dynamic mechanical loads due to the acoustic pressure waves. The common materials used for making MEMS membranes are silicon nitride and silicon oxide thin films. The stoichiometric low pressure chemical-vapor deposition (LPCVD) nitride thin film has a tensile stress of over 550.75 MPa and 0.3 μm of an oxide film has a compressive stress about 429.49 MPa [36]. If the thin film of the membrane is deposited with a resulting high compressive residual stress, the released membrane will buckle and collapse [37]. On the other hand, high tensile residual stress renders the membrane mechanically very stiff, resulting in possible rupture [37]. Therefore, a composite laminate membrane of alternating nitride and oxide films can be made in which the tensile stresses due to the nitride and the compressive stresses due to the oxide balance each other and result in lower net residual stress.

Table 2-1 Estimated residual stress and Young's modulus [15]

Materials	Residual Stress (MPa)	Young's Modulus (GPa)
Silicon Oxide	-429.49	54.59
Silicon Nitride	550.75	270.54

It is difficult to fabricate thick (> 5 μm) composite membranes of silicon nitride and silicon oxide. Pin-holes defects are generally formed while depositing thicker layers, which degrade the membrane properties and operation. Thus, instead of making a composite membrane, silicon was explored as a potential membrane material. Silicon wafers used in the micromachining process are almost defect-free and do not have any residual stresses. Silicon can also be reduced to any desired thickness by standard

micromachining processes, which is important to tune the dynamic properties of the membrane.

Finite element modeling

A finite element model developed using Comsol Multiphysics™ 3.3 was used to determine resonant frequency of membranes of different materials and dimensions. Mindlin plate theory was used for the eigen-frequency analysis of a clamped-free-clamped-free square membrane. This analysis allows the dimensions of the membrane for different materials to be selected to have a desired resonant frequency. The magnitude of the response of the membrane should be linearly dependent on the pressure of the acoustic wave and hence it is desirable that its operation range be well below its resonant frequency. If the membrane operates near the resonance even the slightest pressure wave could lead to a large response thus making it difficult to know the pressure of the incident acoustic wave. Table 2-2 shows the response of different membrane materials versus different sizes of the membrane.

Table 2-2 Estimated eigen-frequency with membrane dimensions

Membrane dimensions (mm x mm) \ Thickness	**Eigen frequency (Hz) for different membrane materials**			
	Silicon Nitride 2000 Å	**Silicon Oxide 1 µm**	**Silicon oxide 2 µm**	**Silicon 26 µm**
1 x 1	1890	5874	11746	208100
2 x 2	472	1468	2937	52300

3 x 3	210	653	1303	20300
5 x 5	75	235	470	8360
10 x 10	28	58	117	2090

From the table it could be inferred that the membrane with smaller thickness should be as small as possible in size to have a higher resonant frequency. However the membrane dimensions were chosen to be 1x1 mm^2, 2x2 mm^2, or 3x3 mm^2 based on the constraint of the currently available nanowire substrate dimensions (2 – 10 mm^2). Therefore, a membrane with greater thickness was selected for proof of concept prototype development in order to achieve higher resonant frequency.

2.1.1.2. Magnetic Flux Path

The magnetic flux path between the nanowires and the GMR sensor serves as a bridge for the flow of the magnetic flux lines. It increases the sensitivity of the device by directing the magnetic flux lines to the GMR sensor when the nanowires bend. Various metals and alloys have been investigated that can serve as a good magnetic flux path. The ideal material would be one which has a high magnetic permeability to transmit the magnetic flux lines with minimal losses. Another consideration was to maintain all the magnetic flux lines in plane and parallel to the sensing axis of the GMR chip (explained in detail in section 2.1.1.2.1).This is because the out of plane moments lead to flux leakage. As thin films possess predominantly in-plane moments rather than out of plane moments due to shape anisotropy, a thin film of the chosen material was deposited to connect the nanowires and the GMR sensor [38]. Both elliptical and ring shapes were considered for

the flux path to avoid sharp corners which might increase the leakage of the magnetic flux due to excessive flux concentration [38].

2.1.1.2.1. GMR Sensor

A giant magnetoresistive sensor (GMR) is a magnetic sensor that exhibits a large change in resistance in response to a magnetic field. It is a multilayer device having two or more ferromagnetic layers separated by a nonmagnetic material layer. Electrical resistance of the multilayer changes depending on the orientations of the magnetizations of the ferromagnetic layers. The physics behind the GMR phenomena is based on the spin-dependent scattering of the conduction electrons. The resistance is minimal when the direction of the magnetic moments of the layers is parallel because the possibility of electron scattering at the interface of conductor/ferromagnetic layers becomes smaller. However, if the directions of the magnetizations of the two ferromagnetic layers are opposite, the electron with opposite spin orientation with respect to the magnetization of the electrode layer is scattered, resulting in higher electrical resistance [39, 40]. The characteristic value usually associated with the GMR effect is the percent change in resistance normalized by the saturated or minimum resistance. In those terms, various commercial GMR sensors can achieve a change in resistance as large as 10% – 20% [41]. Due to this large change in resistance in response to the magnetic field, this phenomenon is called giant magnetoresistance. GMR sensors are commonly being used as magnetic read heads in magnetic data-storage media like hard discs because they help in reducing the read access time [42]. A Wheatstone bridge is integrated in the GMR chip, which is

well suited for the measurement of small changes in its resistance when the magnetic field changes.

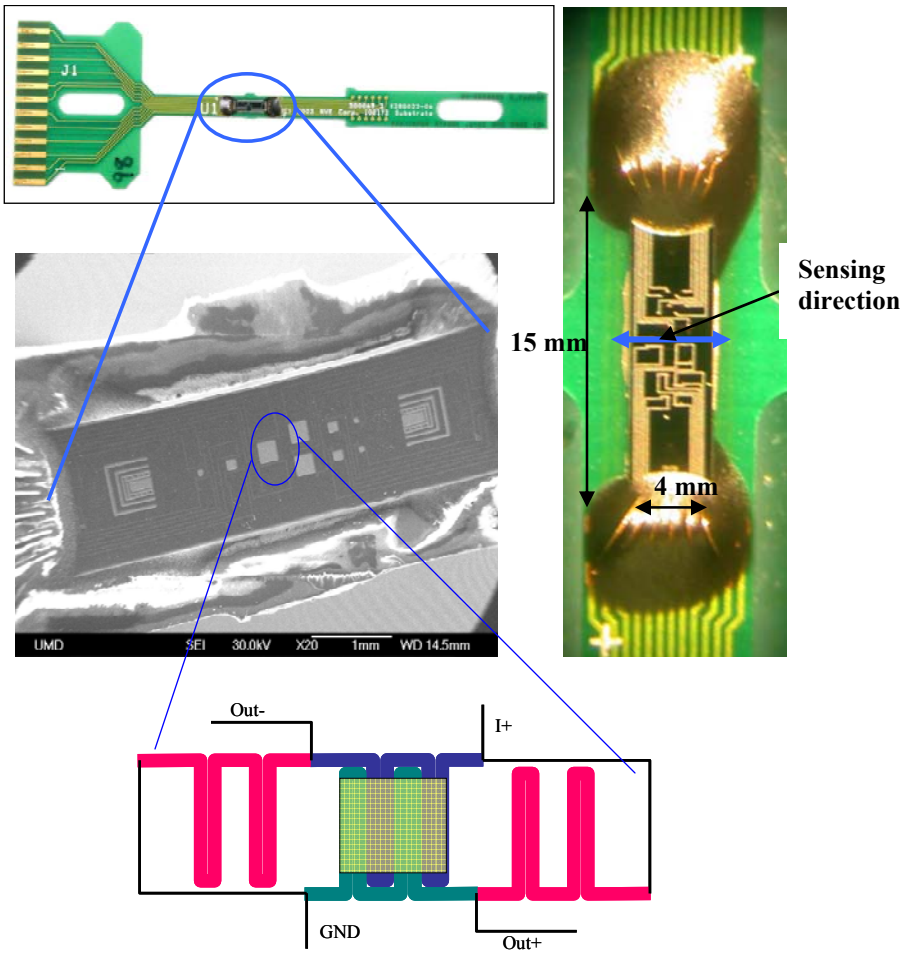

Figure 2.5 GMR "Guitar" chip on a PCB, SEM of the GMR "Guitar" chip, and the wheatstone bridge at the bottom (Pictures courtesy Patrick Downey [43])

As discussed in section 2.1, *Device Structure*, a commercially available GMR "Guitar" sensor (shown in Figure 2.5), has been attached to the nanowire acoustic sensor to convert the change in the magnetic field due to bending of the nanowires to an electrical output. The GMR "Guitar" sensor chip currently available from NVE Inc., Eden Prairie, Minnesota is 15 mm x 4 mm in dimension and was wire bonded to a printed circuit board

(PCB) in the shape of a guitar by the manufacturer. The sensing axis is along the width of the GMR sensor chip, according to the data sheet provided. Due to the limitation of the large size of the GMR chip, it was not possible to place it into the same cavity as the nanowires. It was therefore placed outside the packaging cavity and connected to the nanowires through the magnetic flux path.

2.1.1.2.2. Material selection

Various potential elements and alloys which possess high magnetic permeability were considered for the magnetic flux path, including Nickel, Permalloy: 78% Ni-Fe, Supermalloy: 4% Mo-79% Ni-Fe, and various compositions of Galfenol: $Fe_{1-x}Ga_x$. Magnetic nickel-iron alloys are soft magnetic materials generally called permalloy and they have low magnetocrystalline anisotropy and nearly zero magnetostriction [38]. With the addition of Mo in permalloy, the magnetic permeability is enhanced and the new alloy is called supermalloy. This is because with controlled cooling, the addition of Mo suppresses the formation of the ordered structure after thermal annealing, leading to a large magnetic permeability [44].

NICKEL

Bulk nickel has a maximum relative magnetic permeability of 600 [45] and nickel thin film has about 100 [46]. Although, the permeability is not very large, Ni was considered as the magnetic flux path material because of the availability of well documented deposition and patterning recipes. Ni film can be deposited easily by sputtering, e-beam evaporation, or electroplating whereas most other magnetic alloys are difficult to sputter

in an ordinary sputtering machine. Also, Ni can be easily patterned with a pre-mixed etchant using wet-etching. It has a high melting point of 1453°C [47] and therefore, is not subjected to melting particularly during the bonding of two wafers at high temperature (1000°C) during the acoustic sensor fabrication.

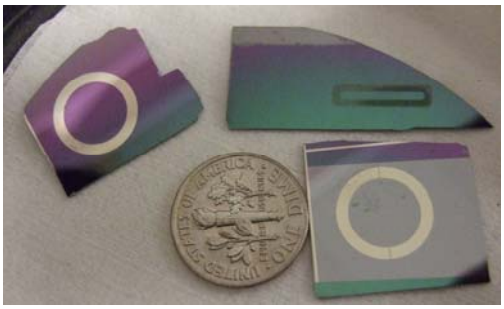

Figure 2.6 Nickel patterned in shape of a ring on silicon and silicon dioxide substrate

SUPERMALLOY

Supermalloy thin film was also investigated for use as the magnetic flux path between the GMR and the nanowires as an alternative to nickel thin film. It was reported that bulk permalloy and supermalloy have very high magnetic permeabilities ($\mu_{max,r}$) of 100,000 and 1,000,000, respectively [48]. The thin films of permalloy and supermalloy have magnetic permeabilities of 4000 and 8500, respectively [49]. Therefore, it was expected that permalloy or supermalloy thin film would be more magnetically responsive than nickel thin film and this would allow the magnetic flux lines to flow without any major losses during the operation of the sensor. A thin film of supermalloy was deposited using an AJA DC Magnetron sputtering machine. The target was bought from Kurt J. Lesker. The film was deposited at a power of 150 W in 5 mT Argon at a base pressure of 9.5×10^{-7} T. The film was patterned in the shape of rings (shown in Figure 2.7) using a lift-off process. Lift-off was used because there is no direct etching recipe available for permalloy.

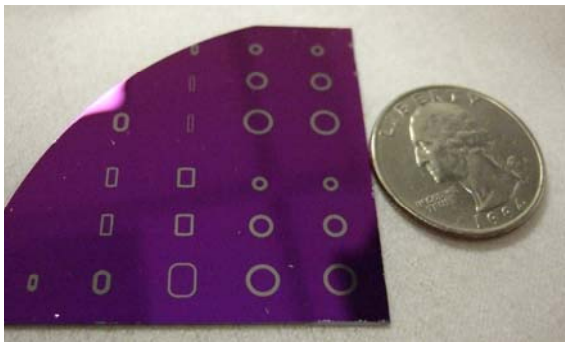

Figure 2.7 Supermalloy patterned in shape of a ring on silicon nitride substrate

2.1.1.3. Packaging Challenges

Packaging plays an especially key role in the effective and reliable operation of the nanowire acoustic sensor, since it is meant for underwater applications. The schematic in Figure 2.8 reveals the major challenges associated with packaging the nanowire acoustic sensor for use in underwater applications. The packaging is not only important to protect the sensor from the harsh underwater ocean environment but also needs to allow the sensor's interaction with the acoustic waves. Sound must be able to penetrate through the package and excite the fluid and the flexible membrane. In order to allow the nanowires to move freely and respond to the incoming sound without any obstruction from the packaging, the encapsulation cannot be made hermetic. At the same time, the package must permit the output of signals from the sensing element to be measured in the form of an electrical output. In addition to that, the package should be able to take mechanical loading due to handling or temperature influences. It must prevent ingression of sea water and salt ions to prevent the corrosion of Galfenol nanowires and GMR interconnects. Besides all this, the package needs to be small and compact.

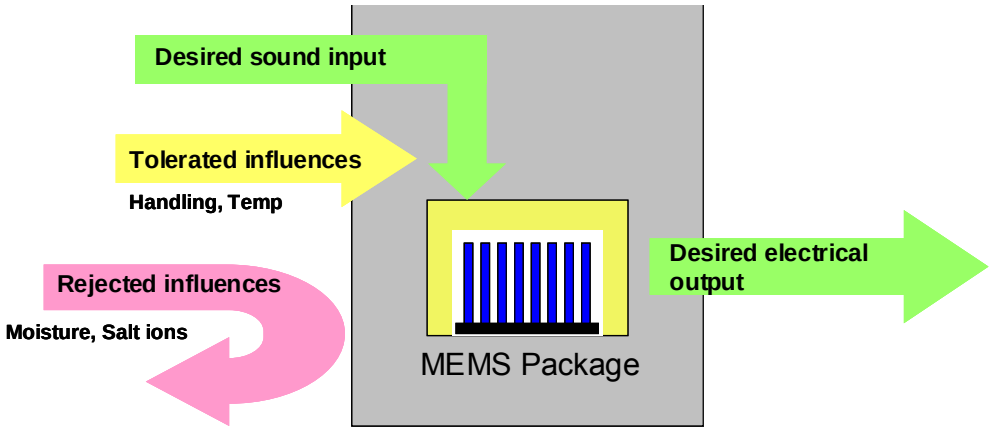

Figure 2.8 Challenges associated with packaging of the nanowire acoustic sensor for use in underwater applications

2.1.1.3.1. Material Selection

Proper selection of the acoustic window material and the liquid medium containing the Galfenol nanowires is vital for the effective operation of the sensor. To allow the sound waves to reach the sensor with minimal losses, both the encapsulant and the liquid are required to have acoustic impedances that closely match to that of sea water. Any mismatch in the acoustic impedance will result in loss of signal due to reflection at the material interfaces. The magnitude of acoustic impedance depends on the density and acoustic wave speed thorough the encapsulant and the liquid, while in an ear, the magnitude of acoustic impedance depends on the mass and stiffness of the tympanic membrane and the frictional resistance offered by the ossicles [9].As the sensor is at the nanoscale, a MEMS package is required and thus there must also be a well established micromachining processes for the chosen encapsulation material. Either inorganic or organic materials can be used for packaging the sensor. A polymer package is preferred over a hermetic one due to low cost, and ease of manufacture at no loss of reliability or ability to withstand the anticipated extreme environmental conditions [50].

Potential encapsulation materials and fluids were identified on the basis of the closeness of their acoustic impedance values to that of sea water. The acoustic impedance (Z) is a function of the material's density (ρ) and the acoustic wave speed (c) through the material according to equation (1). The reflection coefficient (R) for an acoustic wave traveling from one material to another is given by equation (2). If the acoustic impedance of the two media Z_1 and Z_2 are equal, then $R = 0$, which means that the sound wave traveled from one medium to other without any attenuation.

$$Z = \rho \times c \tag{1}$$

$$R = \frac{Z_2 - Z_1}{Z_2 + Z_1} \tag{2}$$

Experimental method

A SONIX Scanning Acoustic Microscope (SAM) with a 15-25 MHz transducer was used to experimentally determine the room temperature acoustic wave speed of each potential material. The acoustic impedance of the medium was calculated after taking the product of its density and the acoustic wave speed through the material, as per equation (1). Several different filler liquids and encapsulation materials were already investigated by DiSabatino [51] and are listed in Table 2-3. Polyurethane rubber (also called rho-c rubber) and castor oil have acoustic impedances of 1.56×10^6 rayl and 1.43×10^6 rayl respectively The acoustic impedances of both these materials closely match the sea water's impedance 1.56×10^6 rayl. However, polyurethane rubber lacks the microfabrication processes essential for the development of a MEMS package. Acoustic properties of encapsulant, SYLGARD 184 (from Dow Corning) and filler liquid, silicon

oil (S159-500, Fisher Scientific) were also studied using a SAM in this thesis. SYLGARD-184, chemically known as PDMS (polydimethylsiloxane) is a two part silicone elastomer consisting of a base and a curing agent. The two components are thoroughly mixed using a weight ratio of 10:1, degassed in a vacuum desiccator for an hour, and cured at 100°C for 45 min. PDMS has not only predefined micromachining processes available but it also has the advantage of being transparent in nature, which aids in alignment with other wafers during the assembly. It is also easy to bond to silicon and glass substrate using oxygen plasma treatment.

Figure 2.9 SYLGARD-184: two part silicone elastomer consisting of silicone resin and curing agent

The test setup used in the SAM consisted of a PDMS sample of fixed thickness to determine the acoustic wave speed through it. The sample thickness was measured with calipers and found to be 2.2 mm thick. The sample was kept in distilled water under the SAM transducer. Using the pulse echo inspection mode, an acoustic pulse was sent to the sample and any portion of sound reflected back at each material interface was recorded as depicted in Figure 2.10. The time *(t)* between reflections A and B shown in Figure 2.11 was measured and the acoustic wave speed *(c)* (in m/sec) in the material calculated by equation (3).

$$c = \frac{2 \times (0.0022)}{t} \tag{3}$$

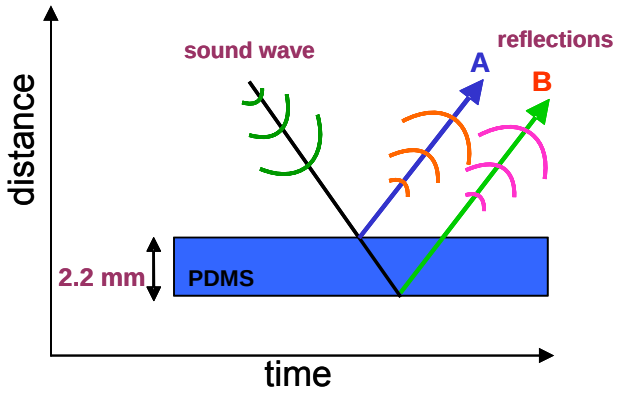

Figure 2.10 An illustration of the SAM testing setup for determining the acoustic wave speed in PDMS

Similarly, SAM was used for calculating the acoustic wave speed through silicone oil. Silicone oil was sealed between a glass bottom slide and a mylar sheet. Two standard glass slides were used as spacers to maintain a constant thickness of the oil. The time difference between reflections at the two oil interfaces was measured and used to calculate the wave speed. Silicone oil was selected because its density is close to PDMS and chemically, it is similar to and compatible with PDMS [52]. To avoid further attenuation of the sound pressure at the PDMS-silicone oil interface, it is necessary that not only their impedances match but also their density and wave speed match individually.

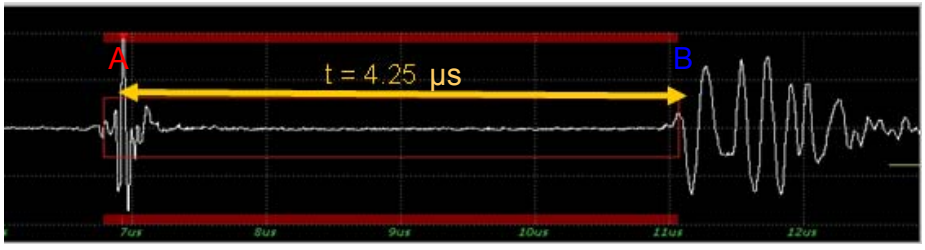

Figure 2.11 An SAM output of the reflection trace through PDMS. Reflection A and B marked correspond to those labeled in Figure 2.10

Results

Table 2-3 Material Properties for Investigated Materials

Material	Density (g/cm^3)	Wave Speed (m/s)	Impedance (rayl x 10^6)
Water (20ºC) [53]	1.000	1483.2	1.48
Seawater (20ºC) [53]	1.025	1522.2	1.56
Silicone oil	0.963	1000	0.96
Ethylene Glycol [51]	1.12	1660	1.86
Castor Oil [51]	0.969	1490	1.43
Polyurethane Rubber [51] (rho-c rubber)	1.04	1500	1.56
Polydimethylsiloxane (PDMS/Sylgard184)	1.03	1027	1.05

The acoustic impedances of PDMS and silicone oil obtained experimentally using the SAM closely match each other but are not the closest match with that of sea water (Table 2-3). However, PDMS has the advantage of having well established micromachining processes and hence it was chosen even considering the small reflection of the sound pressure at the PDMS-seawater interface (R = 19.54%). Acoustic testing done to evaluate the performance of these materials with respect to other encapsulant materials and filler liquid media is described in Chapter 4.

2.1.2. **Electromagnetic interference effects**

An important issue to be addressed in the design of the magnetostrictive nanowire based acoustic sensor was to minimize the electromagnetic interference (EMI) effects. The electromagnetic waves can interact with the nanowires, the magnetic flux path, and the magnetic sensor, thus interfering with the sensor performance. If all three of them are placed inside a diamagnetic material (like silicon, pyrex), they can be shielded from the external magnetic fields and EMI. This is because, the internal magnetization of the diamagnetic materials points in a direction so as to oppose the external magnetic fields. The sensor design consists of a deep silicon cavity in which nanowires and the magnetic sensor are placed, which is bonded to the pyrex wafers on both the sides. Both silicon and pyrex are diamagnetic materials. Water surrounding the packaged sensor is also a diamagnetic material, which helps in shielding the sensor from the EMI effects. In addition, PDMS package is also expected to shield the sensor from these external magnetic field intrusions. Due to the use of these diamagnetic materials and using the sensor for underwater applications, the effect of EMI is minimized.

All the key components – flexible membrane, magnetic flux path, and impedance matching materials are tested individually to verify if the material selection was correct. The experimental setup and the observations for testing the flexible membrane, magnetic flux path, and the external packaging are discussed in Chapter 4. The process sequence for the fabrication of the prototype nanowire based acoustic sensor along with its packaging is discussed in Chapter 3.

3. PROCESS SEQUENCE

The fabrication of the prototype nanowire acoustic sensor using micromachining technology was a major challenge. Its fabrication involves sensitive processes, including fabrication of the membrane, placement of Fe-Ga nanowires, bonding of the lid on the device, and external packaging of the device. Successful fabrication of the prototype sensor requires following proper precautions and inspection at each and every step.

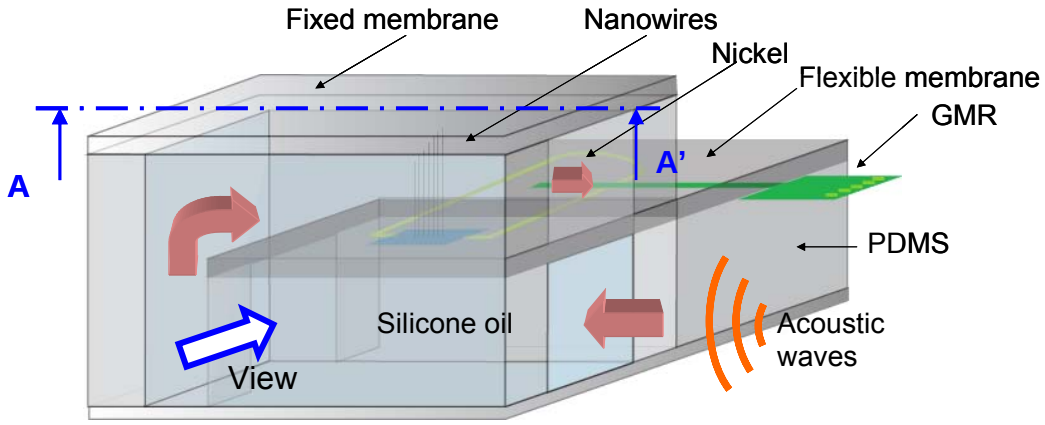

Figure 3.1 The cross-sectional view A-A' are shown in the process sequence for the fabrication of nanowire based acoustic sensor

The fabrication sequence of the nanowire acoustic sensor is discussed below. The real views and the schematics of the cross-sectional **(A-A')** view of the device are included in the fabrication sequence. The figures are not drawn to scale for better visualization. Actual size masks (mask 1 – 6) are attached in appendix A. The color code used for depicting various materials is also included.

Color code:

	Silicon		**Nickel/Supermalloy**
	Silicon dioxide		**Indium**
	Pyrex		**PDMS**
	Photoresist		**Silicone oil**

1. Start with an oxidized silicon wafer

Wafer: Single crystal, 4" p-type (100), 500 μm in thickness, single side polished (SSP) silicon wafer coated with 2 μm thick silicon dioxide layer on both sides. The wafer was thoroughly cleaned with acetone, methanol, and isopropanol, rinsed with DI water, dried, and heated on the hot plate at 95°C for 90 sec.

2. Etching of oxide

The wafer was spin-coated with HMDS (hexamethyldisilazane) before the deposition of resist to help the resist adhere to the oxide. Shipley 1813 positive photoresist was spin-coated on front side of the wafer at 4000 rpm for 40 sec. The wafer was soft-baked on the hot-plate at 95°C for 60 seconds. The resist was then exposed to UV light using mask 1 in the Oriel aligner and was developed for 30 seconds in Shipley 352 developer. Exposing the resist to UV light and developing it transfers the pattern defined by mask 1 onto the resist. The wafer was later hard baked for 2 min at 120°C, which makes the photoresist resistant to etching. The thickness of the photoresist layer was around 1-1.3

μm when measured by profilometer. Following the process described above, the bottom side of the wafer was also spin-coated with the resist. Using an EVG 620 back-side aligner, the bottom side was patterned with mask 2 and the wafer was hard baked to make it ready for the oxide etching.

Next exposed oxide on both sides of the wafer was simultaneously etched away using buffered hydrofluoric acid (BHF is 6:1 HF/NH_4F). The unexposed oxide is covered by the patterned photoresist, which acts as an etch mask and hence protects it during the etching. This transfers the desired pattern defined in mask 1 to the oxide film. As an alternative to wet etching in BHF, dry etching could also be used, but it leads to increased surface roughness. As the subsequent steps require the surface to be smooth, dry etching was avoided in this step. The resist was then stripped in Microchem's nano-PG resist-stripper at 85°C, followed by a rinse in isopropanol and DI water.

3. Partial etching of oxide

As seen from the design of the device, there are two wafers bonded together to make two channels, one above and the other below the flexible membrane. The bonding of the wafers was done by fusion bonding. For fusion bonding (done in step 6), it is essential to have the surface roughness of the bonding surfaces on the order of 10 nm. Since nickel must be deposited on the front side of the wafer as a magnetic flux path, it was essential that the nickel layer not protrude out of the plane of the wafer, which could impede the bonding process at those areas. Thus, a pit was etched in the oxide layer of the same

thickness as that of the deposited nickel. This permits the nickel to subsequently be deposited into the pit and hence should not affect the smoothness of the top surface of the wafer.

To etch the pit, resist was coated on the front side. The resist was then exposed with mask 3 and developed. The other side of the wafer was also coated with resist to protect the oxide on this side during wet etching in BHF. After hard baking the resist, the oxide was partially etched to the depth of 200-220 nm by time-controlled etching. The resist was then stripped away.

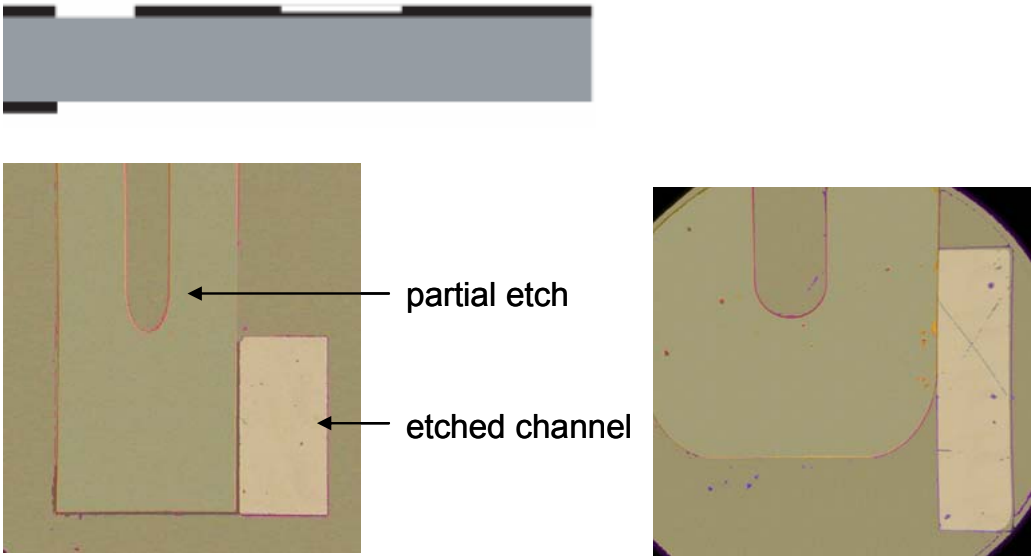

Figure 3.2 The etched channel and the partially etched oxide to bury nickel into it. The figures show the features for 1 mm x 1 mm and 3 mm x 3 mm membrane dimensions

4. (i) Sputtering of nickel

A 200 nm layer of nickel film was sputtered on the front side of the wafer using the AJA sputtering system. The sputtering was done in DC mode at 200 W of power under a vacuum of 5 x 10^{-3} torr. The deposition rate for nickel was 20 nm/min. Deposition of

thicker layers of nickel was also attempted, but resulted in the film flaking-off. Therefore, the thickness was limited to 2000 Å.

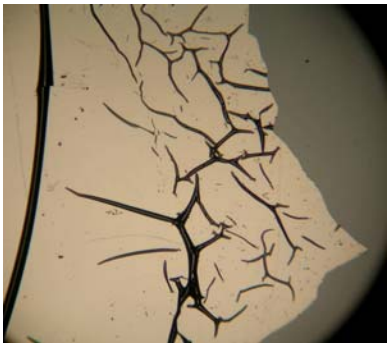

Figure 3.3 A thicker layer of nickel peeled-off at thicknesses greater than 2000 Å

(ii) Sputtering of supermalloy

A 200 nm layer of supermalloy film was sputtered on the front side of a silicon nitride substrate as an alternative to nickel on a second wafer sample. DC magnetron sputtering of supermalloy was done at 150 W, base pressure of 1.7×10^{-7} Torr and argon pressure of 5 mTorr for an hour. The deposition rate was determined as 4.5 nm/min after performing profilometry on the test samples. The thickness was limited to 200 nm because of the slower deposition rate.

Before sputtering supermalloy, photoresist was spin-coated on the front side and patterned with the negative version of mask 4 for a lift-off process. Lift-off was necessary because there is no pre-established etching recipe available for supermalloy. In a lift-off process, the photoresist is patterned first using photolithography and subsequently, a film usually metallic, is deposited on top of it. Later the photoresist is removed with acetone,

taking the film over it and leaving only the film that was directly deposited on the substrate to form the final patterns on the wafer.

After supermalloy was sputtered, the wafer was soaked in acetone for 15 min to completely dissolve the resist, exposing supermalloy rings. It should be noted that for an easier lift-off process, as a rule of thumb, the pre-patterned resist should be more than 1μm thicker than the deposited layer of the metal.

5. Etching of nickel

The resist was coated on nickel and exposed using mask 4. After hard baking, nickel was patterned with a transene nickel pre-mix etch with an etch rate of 0.4 nm/sec. As depicted in the cross-sectional view, nickel was left buried in the pit.

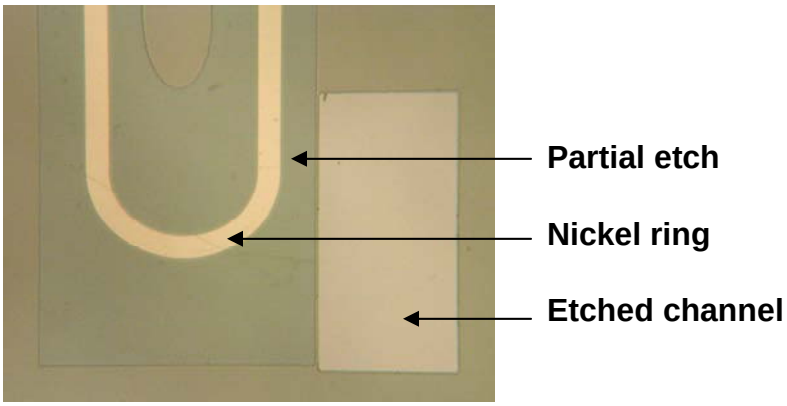

Figure 3.4 The etched channel and the nickel ring in the partially etched silicon oxide

The supermalloy shown in Figure 3.5 was patterned using a lift-off process as described in step 4.

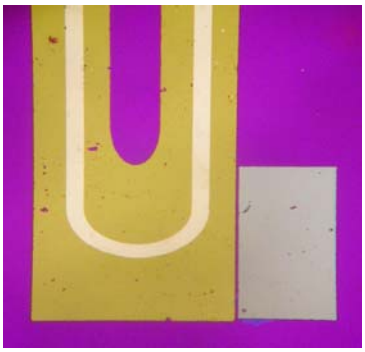

Figure 3.5 The etched channel and the supermalloy ring in the partially etched silicon nitride.

6. Fusion bonding to a second silicon wafer

Next, a 4" p-type (100), 100 µm thick double side polished (DSP) silicon wafer was bonded to the original wafer. A thickness of 100 µm was chosen because the available nanowires are 100 µm in length and hence they will touch the lid that will be placed on this silicon wafer in the subsequent steps. It is essential that nanowires touch the lid as it is due to the shearing of these nanowires against the lid (fixed membrane) that a change is induced in the magnetic flux density.

Fusion bonding of this wafer and the wafer from step 5 was performed. No alignment was necessary when placing the wafers over each other as the 100 μm thick wafer did not have any patterns on it yet. This eliminated the possibility of getting dust particles on the surfaces of the wafer to be bonded during aligning. The wafers were cleaned and kept in direct contact with each other on the working bench. Later they were placed in the wafer bonder EVG 501 for fusion bonding.

Fusion bonding was a very challenging step as it was difficult to achieve void-free bonding when there were patterns on one of the bonding sides. A rigorous cleaning procedure was followed prior to bonding, which is critical to achieve good fusion bonding. Cleaning of the bare silicon wafer prior to bonding was performed in a standard 1:1 H_2S0_4:H_20_2 Piranha solution to remove the organics, followed by a 1% HF dip to remove oxides from the surface. In addition, the wafer was activated in oxygen plasma in a Reactive Ion Etching system (RIE). The wafer was given a 60 sec plasma treatment with 10 sccm (standard cubic centimeters per minute) O_2 flow rate, at a power of 100 W and 30 mTorr base pressure. The other wafer which has nickel on it could not be cleaned using the common approaches of either Piranha solution or HF. This is because Piranha solution etches nickel and HF can etch the oxide on the wafer, which is an etch mask for making the flexible membrane. Therefore, the wafer was only treated in oxygen plasma with process parameters similar to the bare silicon wafer. After the plasma treatment, the activated wafers were immediately rinsed in DI water and spun dry for another 5 min in a conventional tabletop spin dryer. Finally, wafers were brought into contact while providing pressure through tweezers moving from the wafer center to the rim to initiate the bonding wave. No additional force was applied to the wafers. The wafers were kept in

the wafer bonder for an hour. A force of 1000 N and a temperature of 400°C were then applied on the wafer in the wafer bonder. The wafer was later annealed for an hour at 1000°C directly after bonding. This process step is crucial for reliable bonding as it allows the oxide layers formed as a result of high temperature to diffuse into each other. Since both nickel and supermalloy have melting points above 1400°C [47], there was no concern annealing the wafer at such high temperature.

The bond strength was checked by inserting a blade between the two wafers. The wafers were parted only close to the rim, which indicated a strong bond in the middle where the actual devices were present.

7. Deposit indium solder

Indium thin film was used as a solder for bonding either a pyrex or a silicon lid on the device, to act as a fixed membrane. As indium does not have a pre-mix etch, lift-off was used to pattern it. A thick layer of photoresist was spin-coated on front side of the wafer and exposed with the negative of mask 5 using the EVG 620 aligner. Thin films of nickel and indium were then deposited on the front side. Nickel served as the diffusion barrier as well as the wetting layer during solder bonding. The nickel was 150 nm thick while the indium was 2 μm thick. Both of them were deposited using a thermal evaporator. During lift-off, the resist was dissolved in acetone exposing indium solder. Subsequently and

similarly, the back side of the wafer was also spin-coated with resist and coated with Ni/In for lift-off process. The negative of mask 6 was used for patterning the back side.

Indium solder has the advantage of achieving a bond using a cold-welding process at room temperature. The problem with indium is that it oxidizes quickly which impedes bonding. The process steps for achieving a strong bond are to clean the indium coated wafer in dilute hydrochloric acid (10:1 HCl) to remove the oxides and then press the two wafers together with finger tip force to achieve the bonding. Indium is such a soft metal that it diffuses well together when pressure is applied. Alternatively, after cleaning the indium coated wafers, eutectic bonding can also be done by heating the two wafers to a peak temperature of 180°C, slightly more than the melting point (157°C) of indium with force applied on the two wafers during reflow. It is expected that this temperature should not affect the nanowires because the melting point of Galfenol ranges from 1370°C to 1480°C as the percentage of gallium decreases in the alloy from 27% to 17%. Still cold welding is preferred over eutectic bonding, as it is equally reliable and can be easily performed at room temperature, while no flux is required.

8. Silicon etching on the front side

The silicon wafer was etched from the front side in the STS deep reactive ion etching (DRIE) system to form the cavity in which the nanowires must be placed. The thick photoresist SPR 220 7.0 was used as an etch mask. An 11 µm thick resist was coated on the front side of the bonded wafer, which is sufficient to last during the through-etch of the silicon wafer. Before etching silicon, the resist was exposed with mask 5 using the EVG 620 aligner. The wafer was then placed in the STS for DRIE. The etch rate of silicon was 4 µm/min. The DRIE stops automatically when the silicon oxide layer is reached. Hence, oxide acts as an etch stop. In Figure 3.6, the etched channel of silicon on the second wafer is shown. This was patterned for fluid circulation in the device. The nickel or supermalloy ring can also be partially seen on the surface.

The back side of the wafer was also coated with thick SPR 220 resist (11 µm) over indium to serve as an etch mask during deep reactive ion etching of the silicon back side. It was patterned with mask 6 using the EVG 620 aligner.

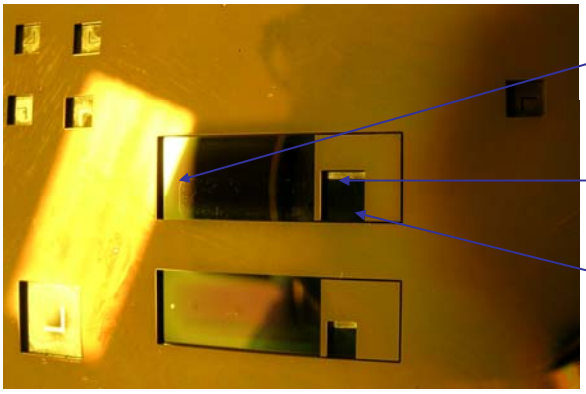

(a)

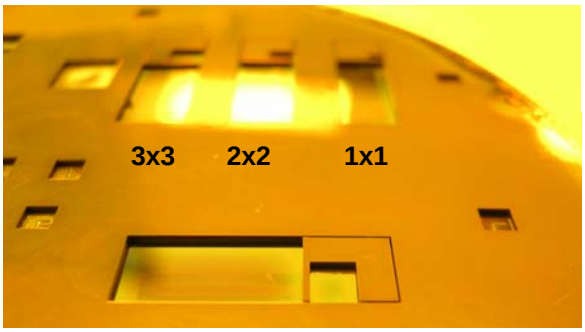

(b)

Figure 3.6 (a) View of the device when silicon has been etched from the top. Nanowires were not yet attached. (b) The wafer show devices with 1 mm x 1 mm, 2 mm x 2 mm, and 3 mm x 3 mm membrane dimensions

9. Attach Fe-Ga nanowires

The Galfenol nanowires on their substrate were glued onto the nickel or supermalloy layer using a tiny glob of negative photoresist (SU-8). SU-8 was used because it is difficult to dissolve in any solvent. Using tweezers, nanowire substrate was carefully placed in the small cavity on the wafer.

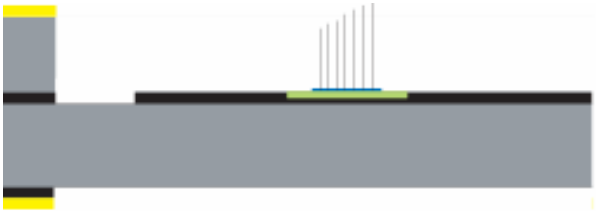

10. Bond pyrex/silicon wafer

Some pyrex/silicon lids already pre-coated with Ni/In and diced were placed over the silicon cavity containing nanowires. These diced lids were manually placed and bonded on the wafer with the help of a lens, using either a cold welding or eutectic bonding process, as described in step 7. A handle wafer was then placed over these diced lids by spin-coating photoresist for the subsequent step of deep silicon etching from the back side in STS to release the membrane.

The lids were pre-diced because it was not possible to dice the entire device after the fabrication of the membrane. Water is used as a cooling agent during the process of dicing which could completely shatter the membrane, because of its high surface tension.

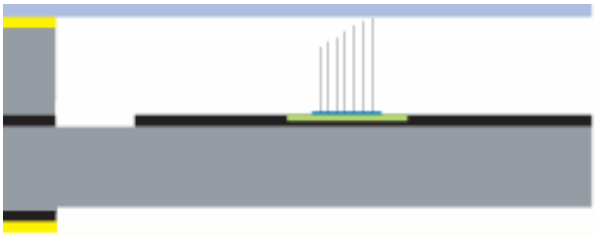

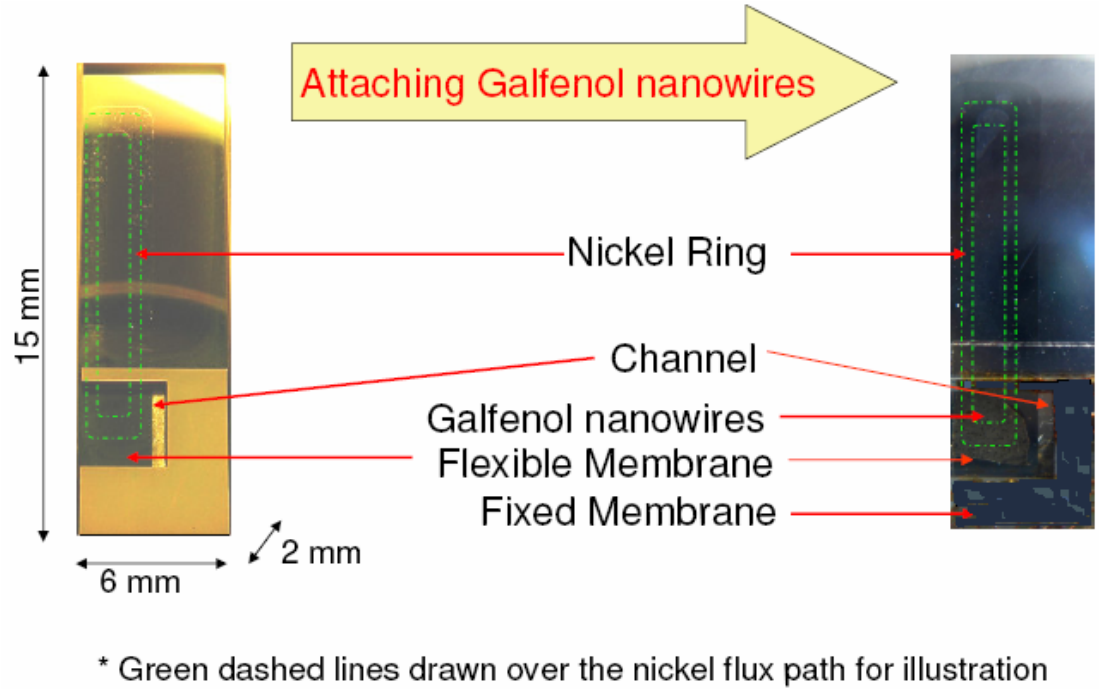

Figure 3.7 Prototype sensor after attaching Galfenol nanowires

11. DRIE of silicon to release the membrane

Deep silicon etching was done on the back side in STS DRIE. During early fabrication, a 3 mm x 3 mm and 2 µm thick oxide membrane was fabricated, but the residual compressive stresses were too high and shattered the membrane completely. Similarly, a 3 mm x 3 mm and 200 nm thick nitride membrane was also ruptured as it was too thin and large in size to withstand the residual stresses. Additionally, membranes supported only on two sides have a higher susceptibility to ripping. Therefore, a membrane of silicon was fabricated in the final device.

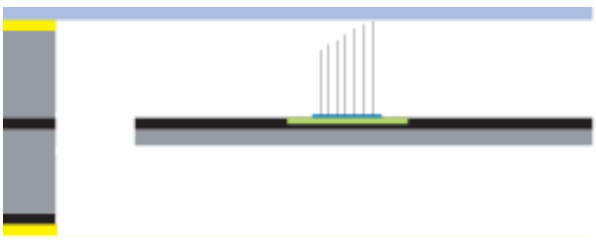

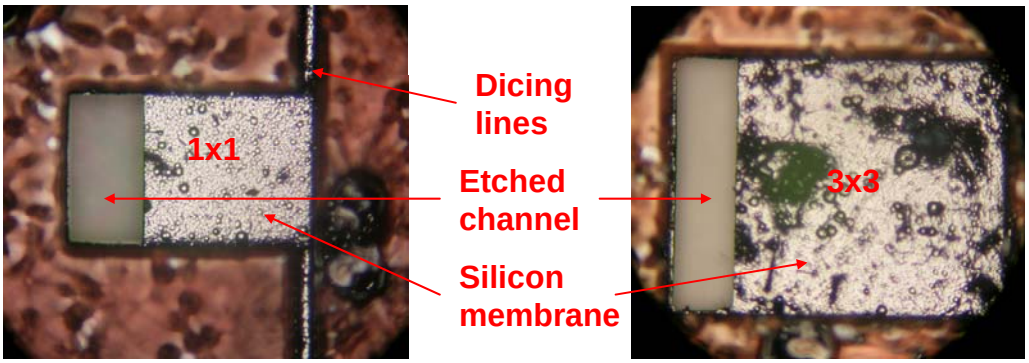

Figure 3.8 Membrane released after back side etching of silicon. The bottom view of membrane shows the etched channel and the dicing lines. The back side of the membrane is not smooth as expected during DRIE. The red background is SPR 220 photoresist not yet stripped away

Figure 3.9 shows the SEM image of the prototype flexible membrane of silicon with an opening on one side, which basically left the membrane supported on two sides. The membrane was 3 mm x 3 mm in area. The side walls obtained after DRIE were straight (90±3°). As the etched depth of wafer by DRIE can only be controlled by etch rate and time, it was difficult to figure out the exact thickness of the membrane during etching. The available profilometer also had limited capability to measure the depth below 160 µm; therefore, SEM (Scanning Electron Microscopy) was used to obtain the thickness of the membrane, which averaged 26 µm.

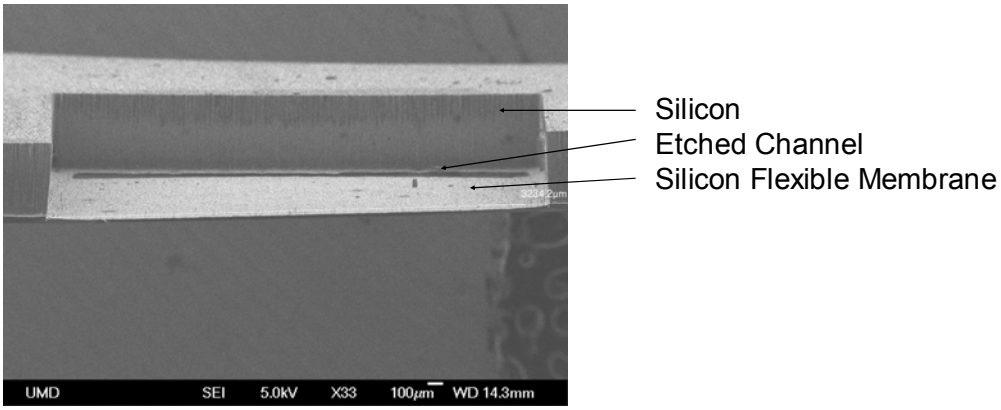

Figure 3.9 SEM image of the flexible membrane of silicon supported on two sides

12. Bond pyrex/silicon wafer

Dicing lines were patterned on the device during photolithography, which were etched into grooves during the DRIE of silicon. The masks for the device (shown in appendix A) contain small etched lines that define the edges of each device. These etched lines were included in the design as this eliminates the necessity to dice the wafer after etching, which has the potential to break the membranes. With the method chosen, the device would easily break free from the substrate along the grooves.

After soaking the device in acetone for 2 days, the devices separated along the dicing lines and were suspended in the solvent. Precautions must be taken, however not to rinse these devices with water and blow dry with nitrogen gas. The devices were carefully left in air for natural drying after taking them out of the acetone.

The last step was to place a lid on the back side to complete fabrication of the sensor. After cleaning the device with dilute HCl, the back side of the device was bonded to a pre-diced Ni/In coated lid applying a small uniform pressure on the sides of the device. This resulted in the final sensor ready to be encapsulated. The process steps for encapsulating the sensor are described in steps 13-14.

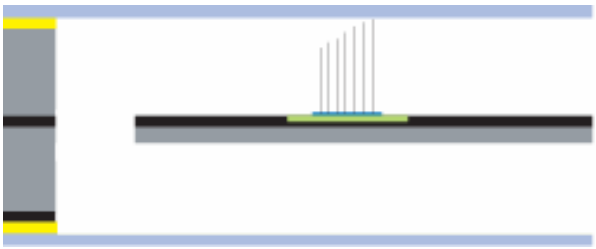

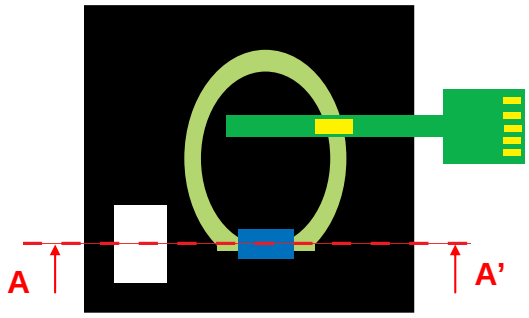

Figure 3.10 Top view of the sensor after assembling with GMR

13. Making a PDMS package

Although micromachining techniques are available for PDMS, the packaging requirements made it acceptable to cast it in a conventionally machined mold.

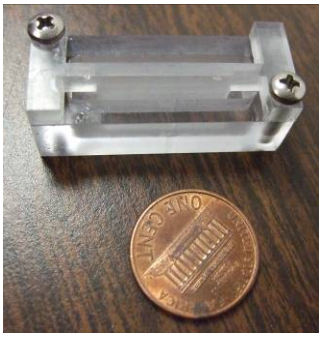

Figure 3.11 Polycarbonate mold for the PDMS package

The mold was made of polycarbonate (Figure 3.11), which is easy to machine and which easily releases cured PDMS without leaving any residue. PDMS resin and curing agent were poured into a weighing boat in the ratio of 10:1. The mixture was mixed well with a wooden stick for 5 minutes and then placed in a vacuum desiccator to degas for about an hour, until all bubbles were eliminated. The mixture was then poured into the polycarbonate mold and cured in a pre-heated oven at 100°C for 45 min.

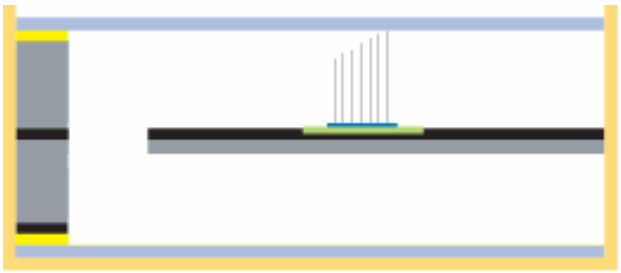

14. Inject silicone oil inside the PDMS package

After releasing the PDMS package from the mold, it was filled to the brim with degassed silicone oil using a syringe. Then the device was placed (snug-fit) inside the slot provided. A lid of PDMS was placed over the opening and overmolded with additional PDMS to get the final packaged sensor. Figure 3.12 shows the sensor enclosed in a PDMS package filled with silicone oil.

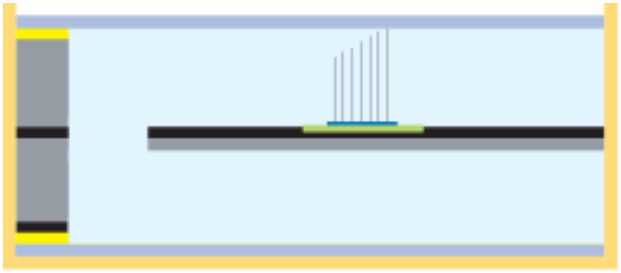

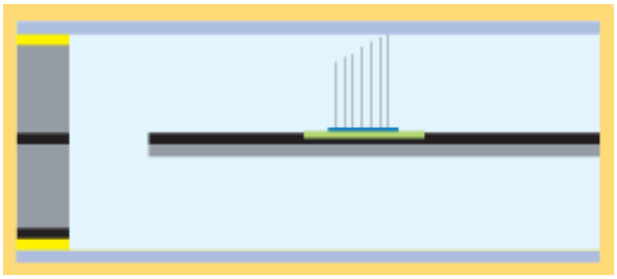

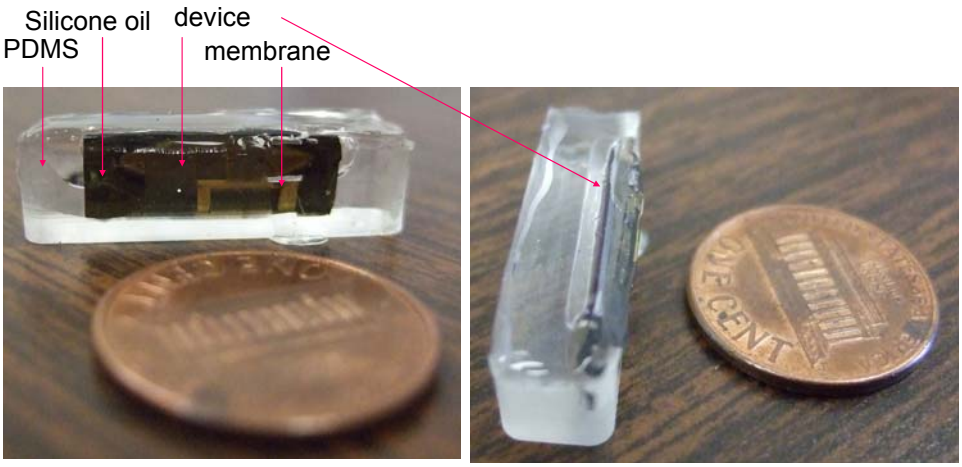

Figure 3.12 Sensor enclosed in PDMS package filled with silicone oil (GMR sensor as not been attached)

Chapter 4 discusses the testing of the key components - flexible membrane, magnetic flux path, and external packaging materials for the nanowire acoustic sensor. Each experimental setup and test procedure has been explained separately along with the discussion of a detailed set of observations and preliminary results.

4. EXPERIMENTAL TESTING

The device is fabricated with all its key components – membrane, magnetic flux path, and external package, as described in chapter 3. In this chapter, testing of each of those components individually is described. Since, the elastic and magnetostrictive properties of FeGa nanowires are still being investigated, the testing of the whole device could not be performed as part of this thesis research and is left for the future. However, testing of each individual component has been performed and it was shown that the components work as intended.

4.1. Membrane testing

Testing of a 3 mm x 3 mm membrane was performed using a Scanning Laser Vibrometer (Polytech PI-OFV056). Laser Vibrometer measurement is based on the Doppler Effect. When a monochromatic, coherent beam of light is reflected/scattered by a moving object, the frequency of the reflected beam undergoes a shift relative to that of the incident beam. This shift in frequency is proportional to the component of the object velocity parallel to the beam axis. Thus, a Laser Vibrometer can be used to get a direct measurement of the target velocity. However, the target must be in the direct line of sight of the beam and should be able to scatter/reflect the beam without significantly reducing its intensity.

Therefore, the device is fabricated without its top and bottom lids. This allows the membrane to be in the direct line of sight of the laser beam. The laser beam is focused on the top surface of the membrane because it is a polished surface and hence is reflective. The other side of the membrane is very rough due to dry etching (DRIE) and was

observed to not reflect the beam at all. The front side, apart from being polished also has a nickel/supermalloy ring on its top, making that portion of the membrane surface even more reflective. The thickness of the membrane averaged 26 μm. As described in section 2.2.1, this should have its first resonant frequency at 20 kHz.

4.1.1. **Test Procedure using Laser Vibrometer**

The membrane was first tested in the air. For this, it was fixed onto a wooden frame with a through hole using double sided tape. The membrane was placed on top of the through hole, which ensured that its motion was not obstructed. The wooden frame with the membrane attached was held in place using a small vice as shown in Figure 4.1 (left). A function generator was used in a sine sweep mode (10 Hz – 25 kHz) along with an amplifier and speaker to generate acoustic waves. The Laser Vibrometer was used to measure the velocity of the membrane as it vibrated due to these acoustic waves. The sensitivity of the Laser Vibrometer was set at 5 mm/sec/V and the voltage output from the vibrometer was read by the computer via a data acquisition system (DAQ). The flowchart in Figure 4.2 shows the sequence for testing the flexible membrane using the Laser Vibrometer.

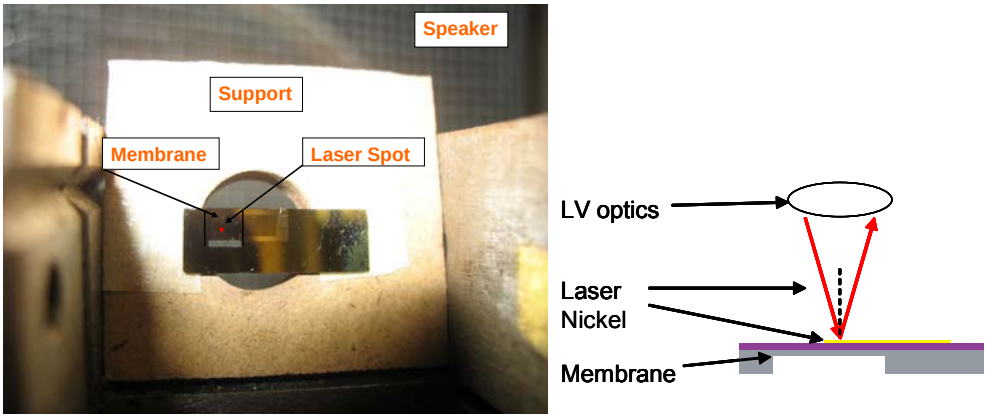

Figure 4.1 A zoomed in image of the membrane held on the wooden frame supported on a vice (left). The amount of light scattered back from the reflective nickel layer on the membrane surface was sufficient for good signal analysis in the Laser Vibrometer (right)

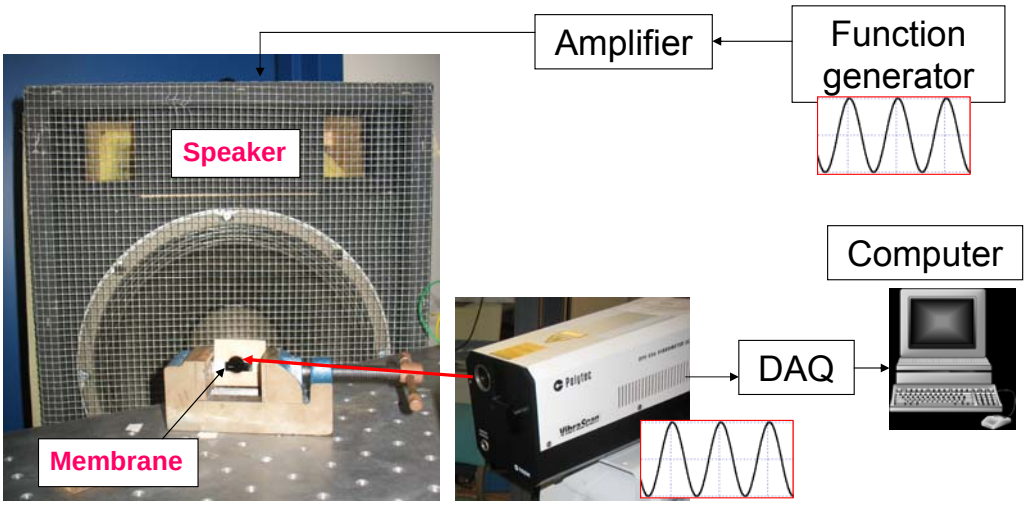

Figure 4.2 The frame with the flexible membrane was held on a vice and a loud speaker was used to generate sound waves for measuring the acoustic response of the membrane with a Laser Vibrometer on the right

Results

The measured frequency response of the membrane is plotted in Figure 4.3(a). It can be observed that apart from a peak at ~19.8 kHz (as predicted by FEM), there are also several peaks at lower frequencies. These peaks could be due to the motion of the whole device because of the motion of the wooden support.

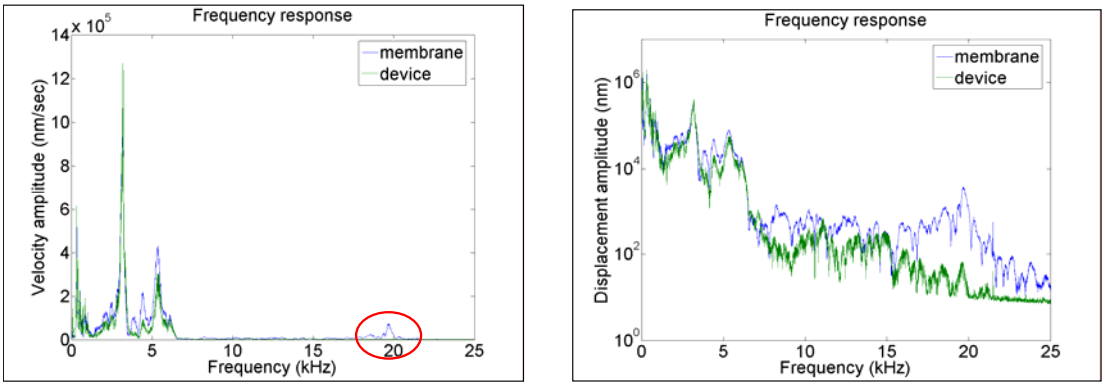

(a) (b)

Figure 4.3 Experimental results showing magnitude of (a) Velocity and (b) Displacement response of the membrane vs. frequency of the sound waves

To corroborate this, the frequency response of the device (with the laser spot off the membrane) was also measured. It can be observed from the plots in Figure 4.3 that the lower frequency peaks appear in the frequency responses of both the device and the membrane whereas the 19.8 kHz peak appears only in the frequency response of the membrane. This indicates that the lower frequency peaks are in fact not due to the membrane motion but due to rigid body motion of the whole of the device itself. To further substantiate this conclusion, the transfer function between the membrane and its supports was calculated and plotted along with the auto spectral frequency response calculations from FEA in Figure 4.4. A unique peak corresponding to the resonant frequency of the membrane can be observed at ~19.8 kHz, which is close to the FEM predicted value (20 kHz).

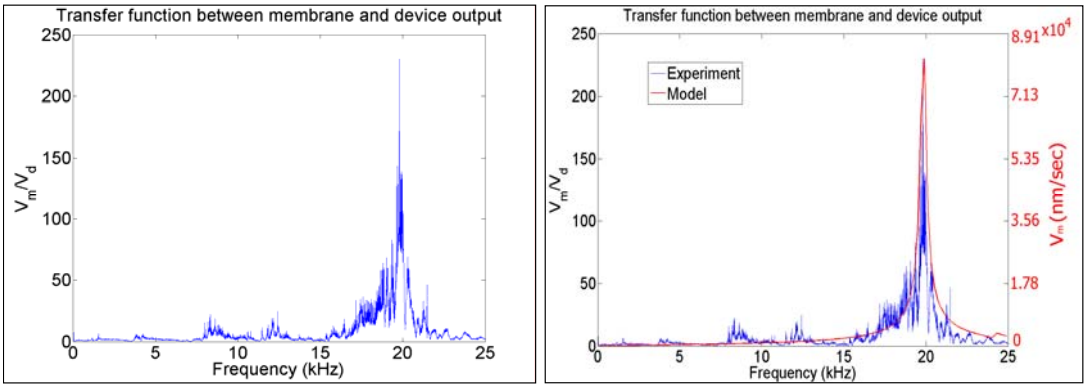

(a) (b)

Figure 4.4 (a) Transfer function between membrane and device output (b) Plot (a) with FEA velocity frequency response function predictions superimposed

Displacement of the membrane *(Δl)* as shown in Figure 4.3(b) was on the order of 100 nm. The length of the nanowires *(l)* was 100 μm. A very basic calculation assuming that the displacement of the membrane does not buckle the nanowires relates the stress in the nanowires to the membrane displacement as in equation (1-2).

$$\varepsilon = \frac{\Delta l}{l} \tag{1}$$

$$\sigma = \mathrm{E} \times \varepsilon \tag{2}$$

Where ε= Strain in the membrane or the nanowires

σ= Stress in the nanowires

E= Young's modulus of bulk Galfenol = 60 GPa

Using the peak sensitivity (20 T/GPa) of macroscale Galfenol samples, this stress level corresponds to a change in magnetic flux density on the order of 1.2 T, which could have been achieved if the experiment has been done using nanowires. A change of 1.2 T can

be very easily measured by any magnetic sensor. However additionally, device and nanowire analysis should be completed before making any firm conclusions.

Based on the preliminary results, the device has potential for use in SONAR applications as well as in devices operating in the audible frequency range. In the case of SONAR applications, the resonant frequency of the membrane can be tuned to match the frequency of operation and thereby increase its sensitivity, although this would be difficult to accurately tune and the increased displacement at resonance would increase susceptibility to fatigue problems. Since the measurements show a flat frequency response of the membrane for frequencies less than 20 kHz, it can also be used as an acoustic sensor in air over the audible frequency range.

4.2. Magnetic flux path

To test the effectiveness of the thin film magnetic flux path, an experiment was designed using nickel thin film on polycarbonate and a GMR sensor as illustrated in Figure 4.5.

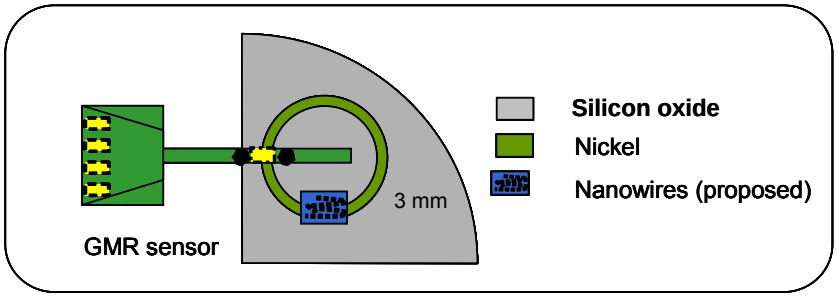

Figure 4.5 Testing of nickel thin film with GMR sensor using (proposed) nanowires

The experimental setup consisted of a polycarbonate ring machined with an outer diameter of 36 mm and a width of 3 mm and having one side coated with 26 nm of nickel film as shown in Figure 4.6. The width of the machined ring was less than the width of

the GMR sensitive chip so that the GMR chip could lie completely across its width. The nickel film on the polycarbonate ring was deposited via e-beam evaporation. The advantage of using nickel is that it is compatible with polycarbonate and has good adhesion properties on plastic substrates [54]. Polycarbonate was used as the substrate because of its insulating characteristics and ability to be easily machined in the form of a circular ring. It has a high melting temperature (approximately 200°C) [54] relative to other thermoplastics, hence it can be kept in any deposition equipment without the problem of melting.

Figure 4.6 Nickel deposited on a polycarbonate substrate shaped in a ring structure

As shown in Figure 4.7, a copper coil was wrapped across the nickel coated polycarbonate ring at two places, one for the drive coil and, one for the pick-up coil. For both coils, gage 30 wire was used to obtain 100 turns and a length of 2.5 cm. When current (I) is passed through the drive coil, the applied magnetic field (H) generated is:

$$H = \frac{NI}{l} \tag{3}$$

The magnetic flux lines (φ) flowing through the nickel film induce a current in the sensing coil by Lenz law, which can be measured.

$$\phi = B \cdot A \tag{4}$$

$$V = -N\frac{d\phi}{dt} = -NA\frac{dB}{dt} \quad (5)$$

$$B = -\int \frac{V}{NA} \cdot dt \quad (6)$$

Where N= Number of turns of the drive coil

I= Current passed through the coil

l= length of the coil

φ= Magnetic flux

B= Magnetic flux density

A= Area of cross-section

V= Voltage across the pick-up coil

In addition to the pick-up coil, a GMR sensor was kept in contact with the nickel film to measure the change in the magnetic flux density (B) of nickel when current was passed through the drive coil. The GMR is configured as a Wheatstone bridge. A change in voltage across the bridge is proportional to the magnetic flux density change that induces a resistance change in the GMR element. The magnetic flux density (B) was calculated from NVE's calibration graph that came along with the GMR "Guitar" sensors.

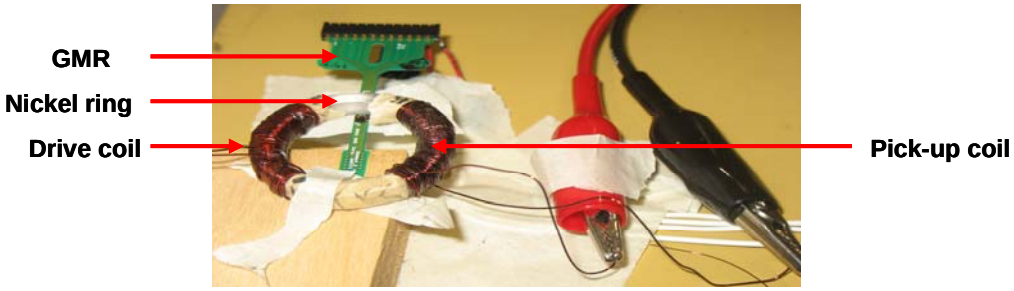

Figure 4.7 A drive coil and a pick-up coil were wounded across nickel film deposited on a polycarbonate substrate to observe the effect of magnetic field on nickel flux path. GMR chip was also placed in contact with the nickel film to take the readings.

The test measurements did not yield any indication of a change in field. SEM examination of the nickel film after the experiment revealed burnt areas of nickel under the locations of the excitation coil (Figure 4.8). Nickel had even flaked off at those locations, which is believed to be responsible for the loss of its functionality as a magnetic flux path.

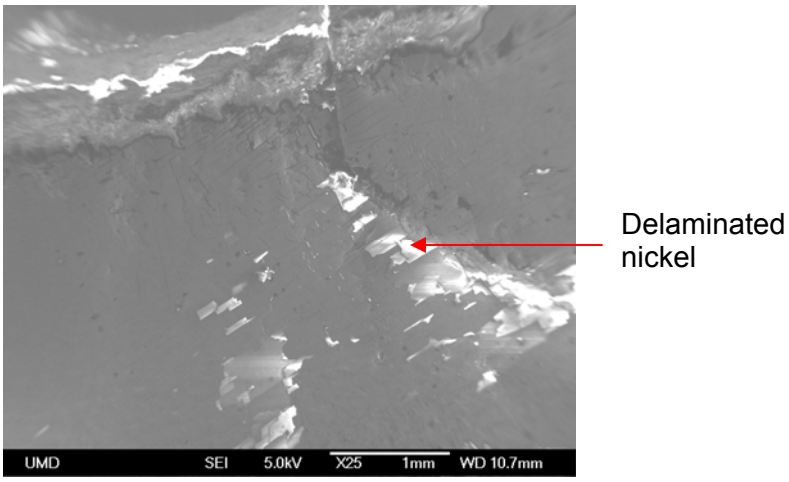

Figure 4.8 SEM image of nickel burnt due to excessive heat generated by the current carrying coil

4.2.1. **Test Procedure using MFM**

A new experiment was designed in which the performance of nickel as a magnetic flux path material was assessed using magnetic force microscopy (MFM). A 200 nm thick nickel film was deposited on an oxide and a bare silicon substrate using e-beam evaporation. The film was patterned in the shape of a small ring as shown in Figure 4.9 using transene nickel pre-mix etch and the magnetic domain structure was inspected using MFM.

MFM detects the changes in the resonant frequency of the probe tip cantilever induced by the magnetic field's dependence on the separation between tip and sample (Figure 4.10 on right). The probe tip is coated with a thin film of ferromagnetic material (Co-Cr) and

when this tip is scanned over a surface, it reveals information about both the topography and the magnetic properties of the surface, including the magnetic domain structure. Since it is possible to apply external magnetic fields during the measurement, the field dependence of domain structures can also be observed. Samples were first tested using MFM with no external magnetic field and later with an applied magnetic field using a permanent magnet of strength 143 mT. The field was externally applied to simulate the magnetic flux density produced due to the bending of the nanowires in response to interaction with sound waves. Here the experiment with no magnetic field was a control experiment.

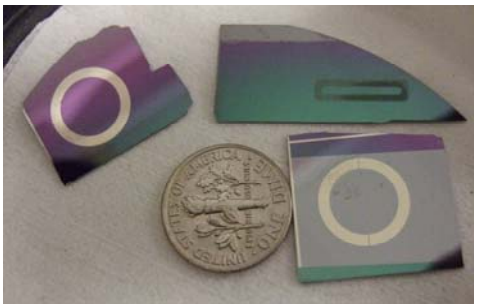

Figure 4.9 Nickel rings deposited on an oxide and bare silicon substrate

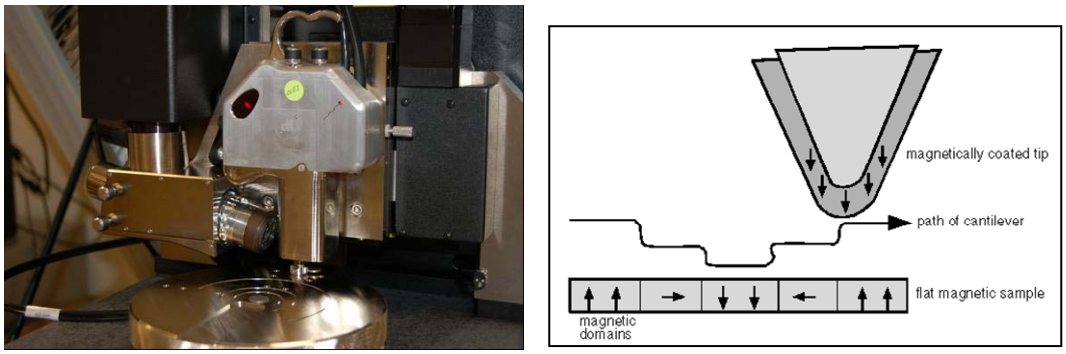

Figure 4.10 MFM setup (left). Schematic of MFM mapping the magnetic domains of the sample surface (right)

Domain walls were observed when the surface of the nickel was scanned at different places using MFM without any externally applied magnetic field. The orientation of the domain walls was dissimilar at different parts of the ring. There was no definite pattern in their orientation. The set of Figure 4.11 and Figure 4.12 shows the height and phase information at two different locations on the nickel ring.

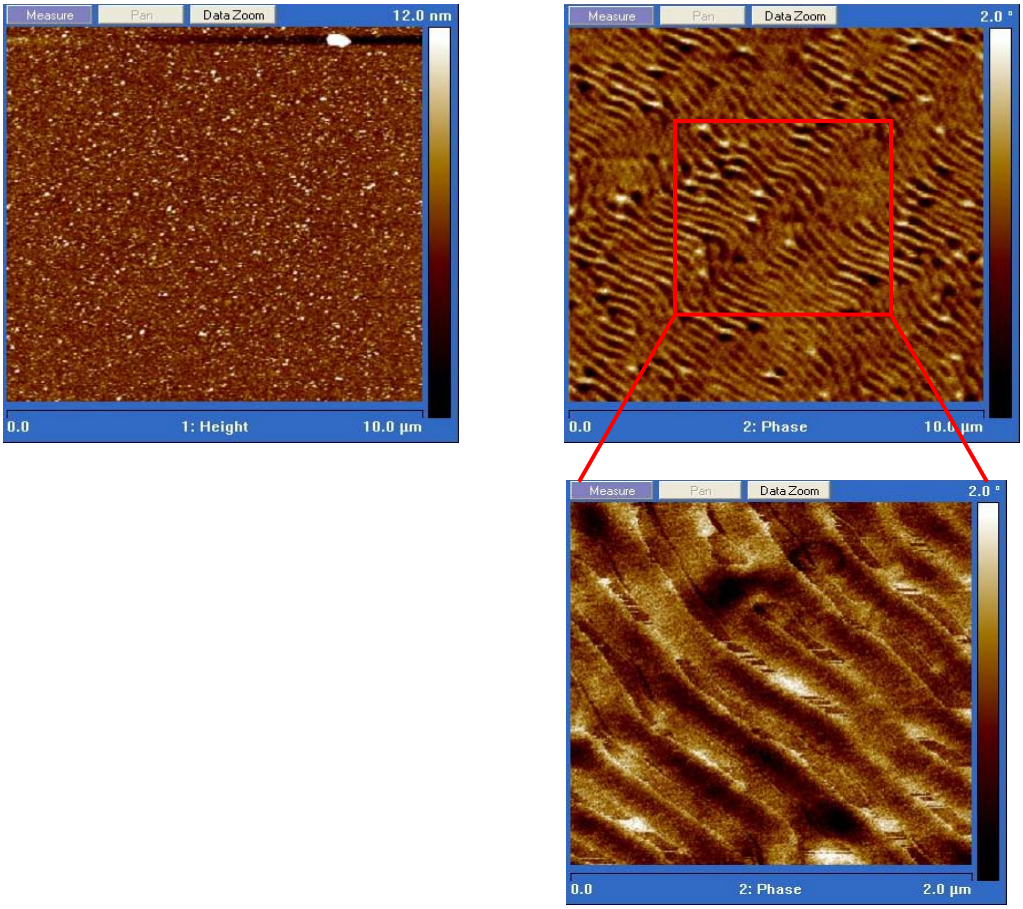

Figure 4.11 Topography and phase information at one location on the surface of nickel thin film. Magnetic domain walls are parallel to each other but oriented at an angle from the horizontal

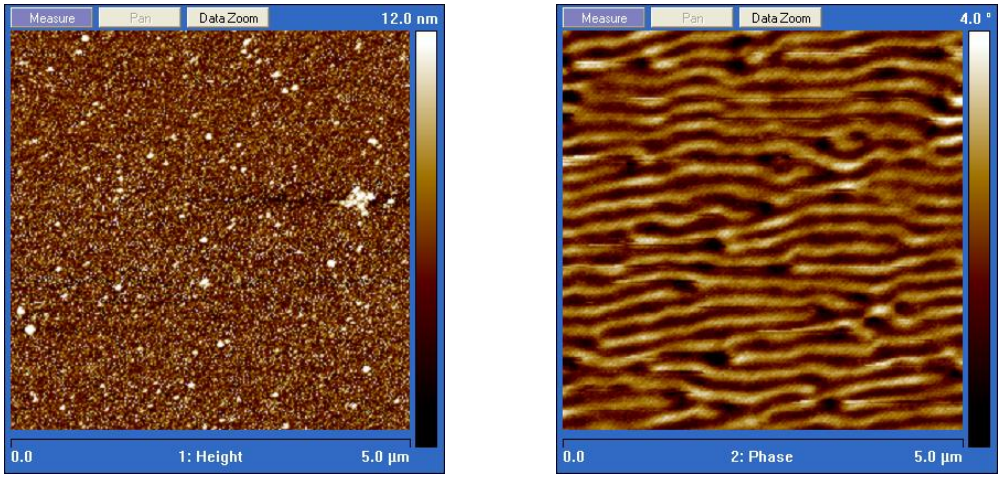

Figure 4.12 Topography and phase information at another location on the surface of nickel thin film. Here magnetic domain walls are also parallel to each other but oriented horizontally

MFM scans were then done again on the same nickel ring with an externally applied magnetic field. A permanent magnet of strength 143 mT was kept below the ring and magnetic domain wall structure was checked at the same locations. There was no difference in the height data of the two MFM scans, but there was an evident difference in the phase data compared with that obtained when no applied magnetic field was present. This change clearly indicated that nickel thin film is magnetically responsive. However, these measurements do not reveal any quantitative change in the magnetic properties of nickel due to the limitations in the scope of the MFM technique. Figure 4.13 shows the height and phase data at the nickel surface with an applied magnetic field.

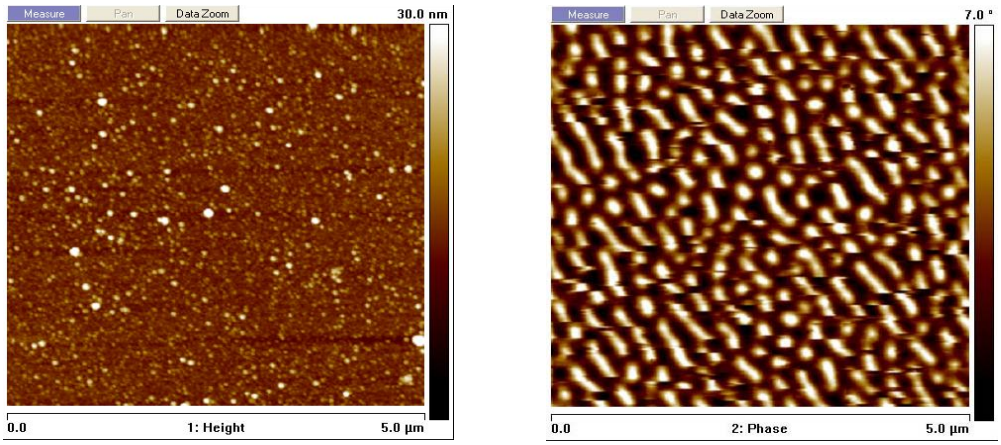

Figure 4.13 Topography and phase information at the surface of nickel thin film with applied magnetic field. Magnetic domain walls look different from the one observed without any applied magnetic field

Thermal Annealing

The nickel magnetic flux path is embedded between the two silicon wafers during fusion bonding, discussed in Chapter 3, which means that it goes through a temperature of 1000°C during bonding. Therefore it was imperative to investigate the magnetic properties of the nickel flux path after annealing at such a high temperature to ensure that the film does not lose its magnetic properties due to oxidation. Also, thermal annealing can reduce the level of defects in the material, thus allowing domain walls to move more easily [55]. It also reduces the internal residual stresses that aid in visualizing the domain walls [55]. Therefore, thermal annealing of the nickel magnetic flux path was investigated to observe its effects on the magnetic properties. The same nickel rings discussed above were thermally annealed in vacuum for an hour at 1000°C in a tube furnace and then furnace cooled. MFM scans were again conducted on these films with and without the externally applied magnetic field using the same permanent magnet.

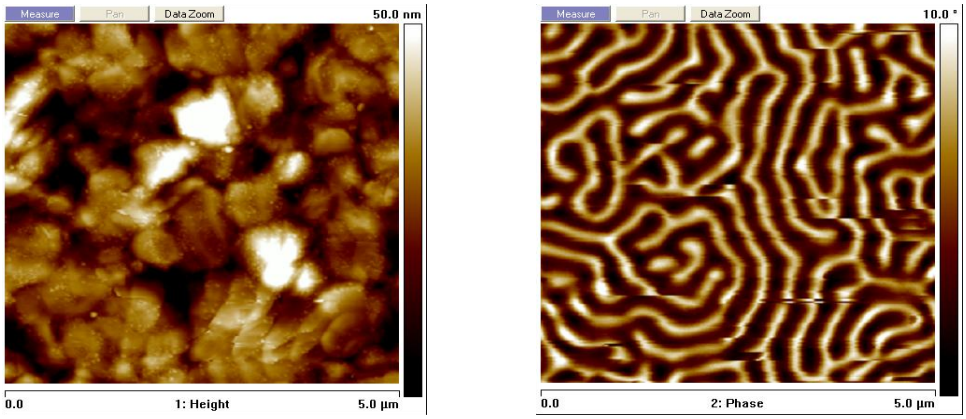

Figure 4.14 Topography and phase information at the surface of nickel thin film after thermal annealing. Magnetic domain walls appear in a finger print pattern

Figure 4.14, reveals that both the topography and phase plots have changed after annealing. The change in the topography can be attributed to the recrystallization and grain growth [55]. This could also be the reason for the changed domain structure to a finger-print pattern from the straight striped domains. When a magnetic field was applied, the MFM scans clearly showed a variation in the phase information while the topography remained the same as shown in Figure 4.15. This indicated that the nickel flux path was responding to the magnetic field even after thermal annealing. However, it is difficult to understand from the measured data if the effect of thermal annealing on the nickel magnetic flux path was positive or negative. It would be possible to measure this effect if there were nanowires.

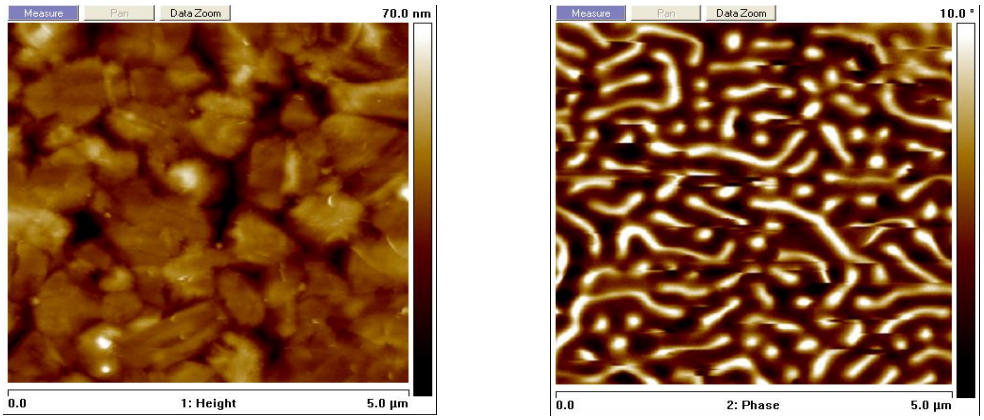

Figure 4.15 Topography and phase information at the surface of nickel thin film after thermal annealing with externally applied magnetic field. Magnetic domain walls look different from the one without any magnetic field

As discussed in section 4.2, a nickel film was deposited on both a silicon dioxide and a silicon substrate. The thermal annealing results discussed above were observed for nickel film deposited on the silicon dioxide substrate. The nickel film deposited on a silicon substrate, annealed at 1000°C in vacuum for an hour and furnace cooled did not reveal anything in its height or phase information as shown in Figure 4.16. This could be because nickel and silicon chemically react at such a high temperature to form nickel silicides [56], which are non-magnetic. Thus, precaution is to be taken not to use a bare silicon substrate for the nickel magnetic flux path. In the current nanowire based acoustic sensor, a silicon dioxide substrate is used for the nickel magnetic flux path. Hence it can be concluded from the MFM tests that nickel film can be used as a magnetic flux path to carry magnetic state changes to the GMR sensor due to pressure induced bending of nanowires. However, the quantitative effects of the intensity of the magnetic field and the thermal annealing of nickel could not be performed and were left for future study.

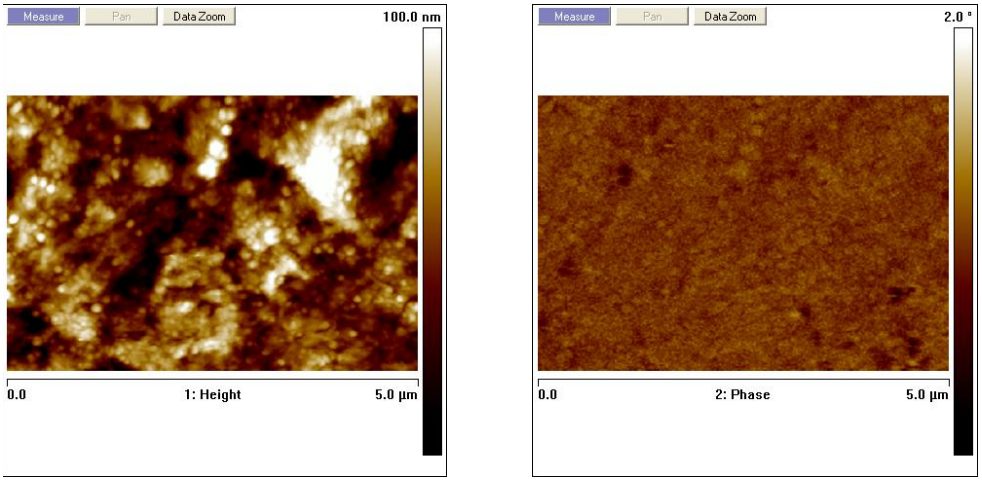

Figure 4.16 Topography and phase information at the surface of nickel thin film deposited on a silicon substrate after thermal annealing. No magnetic domain walls can be observed in the phase data which indicated that the nickel film was no longer magnetic due to the formation of nickel silicide

4.3. Acoustic Testing of the Packaging Materials

The goal of the acoustic testing was to evaluate the acoustic performance of different combinations of the encapsulant materials and the filler fluids for the nanowire acoustic sensor. A test package was designed and fabricated incorporating a commercial microphone from Knowles Acoustics (Part # MR-8406) that was used to perform the function of nanowires, depicted in a schematic in Figure 4.17 and shown in Figure 4.18. The microphone was highly waterproof, corrosion resistant and small in dimensions (12.7 mm diameter). The aim of the test package was to compare its performance with a similar unpackaged reference microphone and thus, select the impedance matching materials for the final sensor package.

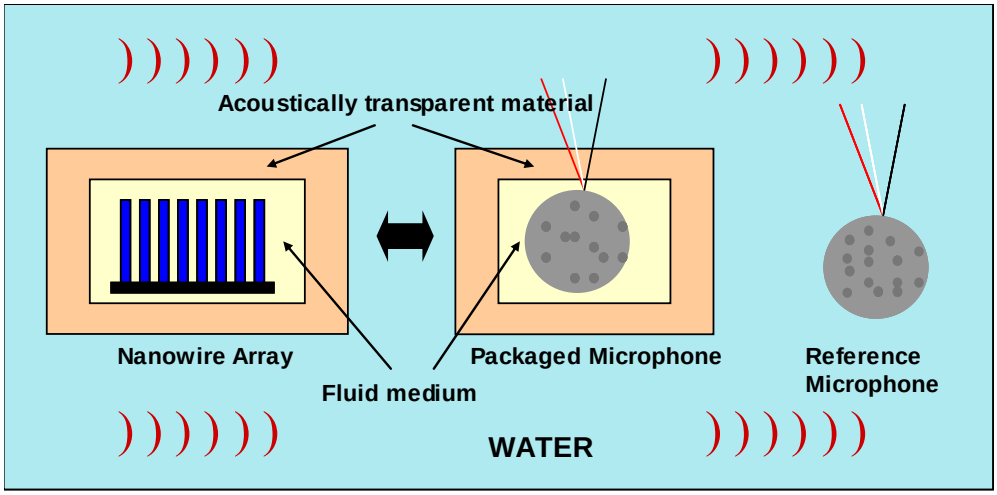

Figure 4.17 Schematic of the arrangement of acoustic test setup with a reference and a packaged microphone. The microphone was used to perform the function of nanowires

Prior work by DiSabatino [51] had included testing of a stainless steel housing but that was found not to be capable of transmitting sound waves at lower frequencies. A polyurethane package was then developed [51] and shown to have a good impedance match with sea water, minimizing the losses at the material interface. Although polyurethane addresses the key issue of matching impedance with sea water to the best possible extent, it lacks well established micromachining processes essential to developing a MEMS package. Therefore packages made of PDMS, which is transparent and has micromachining techniques available were prepared along with those of polyurethane to test and compare their acoustic performance. One of the PDMS packages was filled with castor oil and the other one with silicone oil, while the polyurethane package was filled with castor oil. Each package containing a microphone was carefully sealed by overmolding, making sure that all air escaped the cavity.

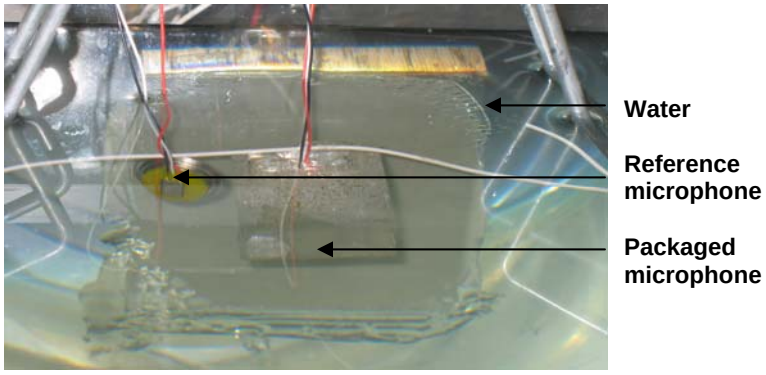

Figure 4.18 Reference microphone and packaged microphone inside water

4.3.1. **Acoustic test setup and procedure**

The acoustic test setup is the one designed earlier [51] shown in Figure 4.19(a). It consisted of a glass tank filled with water and with an aluminum plate attached to one of its outer walls. A threaded hole was drilled in this aluminum plate and one end of a Terfenol-D transducer was inserted into it, while the other end of the transducer was secured to a cinderblock acting as a counter mass using another aluminum plate. The transducer has a magnetic coil around it which produces magnetic field when current is passed through it. A function generator was used to produce a sine wave sweep (10 Hz-10 kHz) with fixed amplitude, which was amplified to drive the Terfenol-D transducer. As a result of the change in the magnetic field, the magnetostrictive Terfenol-D rod vibrates against the wall of the tank generating acoustic waves in the water. The flowchart in Figure 4.19(b) shows the sequence in which sound waves were generated in water using an external Terfenol-D transducer.

The packaged and the reference microphones were hung inside the water filled tank close to the side wall near the transducer at the same height as the transducer. Holding the

microphones far from the side wall where the Terfenol-D transducer is fixed, (e.g. in the center of the tank) decreased the output from the microphone irrespective of the external package material. This is because the sound waves generated by the vibration of all four walls cancel each other at the center resulting in reduced intensity. Data from the microphones were measured using the oscilloscope connected to the data acquisition system. The peak to peak voltages (*Vpp*) from the two microphones were compared at the set frequency range and loss due to the packaging was calculated using the expression below.

$$Loss[dB] = 20 \log_{10}\left(\frac{V_{packaged}}{V_{reference}}\right)$$

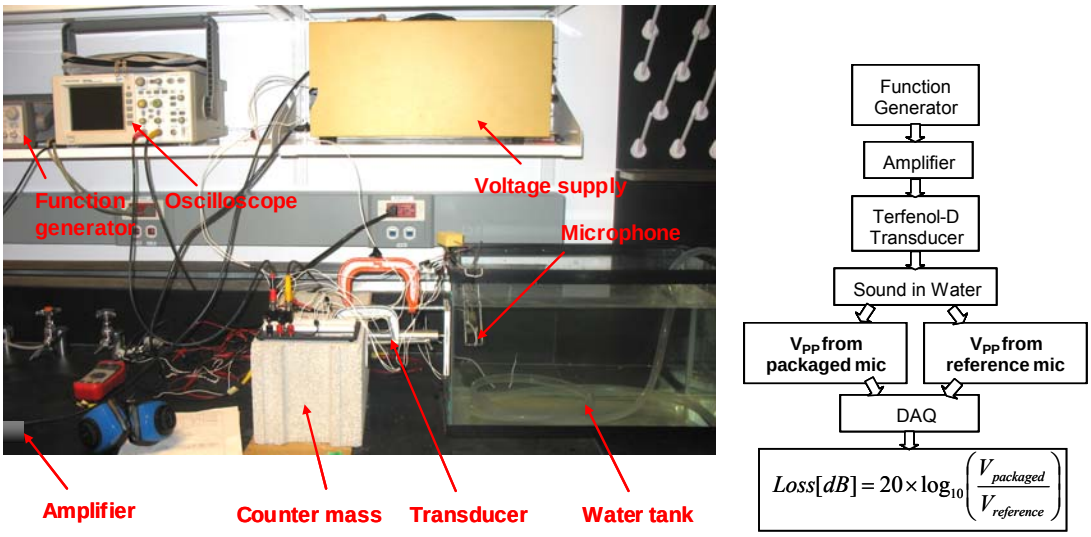

Figure 4.19 (a) Acoustic test setup. (b) Flowchart for performing the steps of the acoustic test

Results

The graph in Figure 4.20 reveals that the PDMS encapsulated package filled with silicone oil performed at par with the polyurethane package while offering the advantage of being

optically transparent. The average loss for the PDMS package with silicone oil was 2.85 dB with a standard deviation of 2.27 dB. It was also observed that the PDMS package with silicone oil had lower losses compared to that of the PDMS package with castor oil especially at lower frequencies. This is likely due to the fact that there is no additional reflection of the sound waves at the interface of the PDMS encapsulant and the fluid medium because PDMS and silicone oil both have the same acoustic impedance.

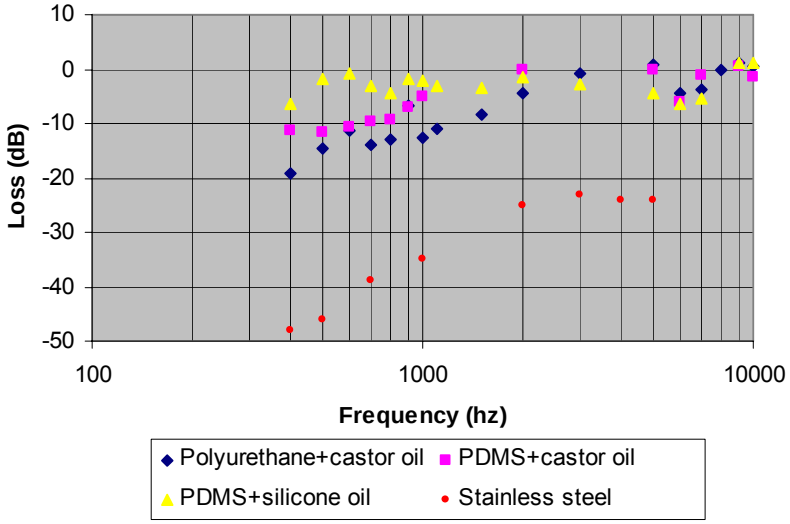

Figure 4.20 Results from the acoustic testing (Loss vs. frequency) for different types of packages

4.4. Moisture Absorption Test

Another important packaging consideration was that the package should not absorb or admit salt water, which has the potential to corrode and destroy the nanowires, magnetic flux path and the GMR interconnects. To test the moisture absorption properties of PDMS, ten cylindrical samples of Sylgard 184 were molded as shown in Figure 4.21, and soaked in a 3.5 wt% salt solution at room temperature for 48 hours. The weights of the samples before and after soaking were measured with a Mettler Toledo AE1000 mass balance with a sensitivity of up to 0.01 mg. The average weight gain for the ten samples

was 0.032 % with a standard deviation of 0.006 %. This was less than 4% of the moisture absorption by polyurethane samples which was found to be 0.85% ± 0.025% by DiSabatino [51]. Another moisture absorption test was conducted at an elevated temperature of 85ºC for both the PDMS and the polyurethane sample immersed in water for seven days. It is expected that the diffusion of water through the encapsulants would increase at such a high temperature. Figure 4.22 shows the percentage change in weight of PDMS and polyurethane samples as they absorb water. At saturation PDMS gained 0.25% weight, which is much smaller than 3% weight gain by polyurethane sample. Thus, the results both at room temperature and elevated temperature indicates that PDMS as an encapsulant material is reliable for use in underwater transducer applications.

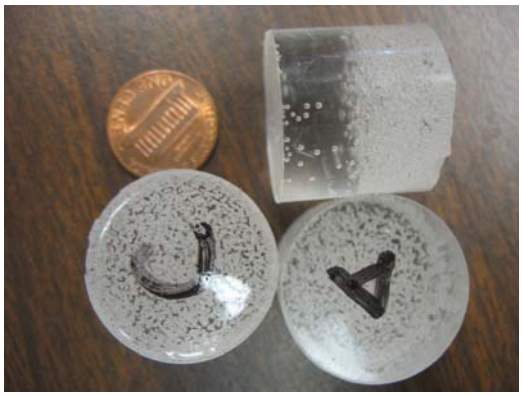

Figure 4.21 Several of the PDMS cylinders used for the moisture absorption test

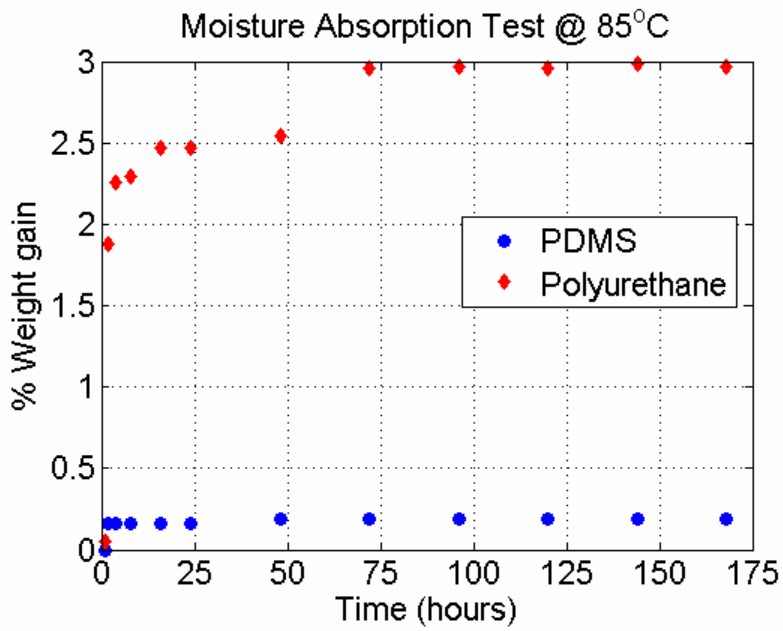

Figure 4.22 Moisture absorption test for PDMS vs. Polyurethane immersed in water at 85ºC monitored for seven days

4.5. Testing of packaged device

The same membrane that was used for testing in air was packaged as described in chapter 3 and attached to the wooden frame held with a vice. The vice was immersed in the water filled glass tank. The setup for testing the packaged device in water was the same as the one used for measuring the acoustic response of the packaging material discussed in section 4.3. A sine wave sweep (2-30 kHz) from the function generator with fixed amplitude was used to drive the Terfenol-D transducer for generating sound waves in the water. The response of the packaged device to these acoustic waves was measured using a Laser Vibrometer.

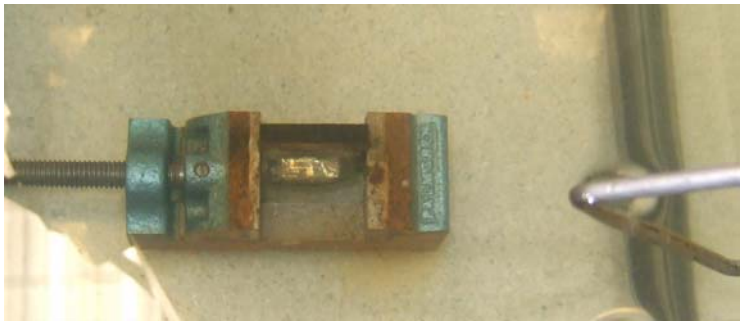

Figure 4.23 Packaged device held on the vice placed inside the water tank

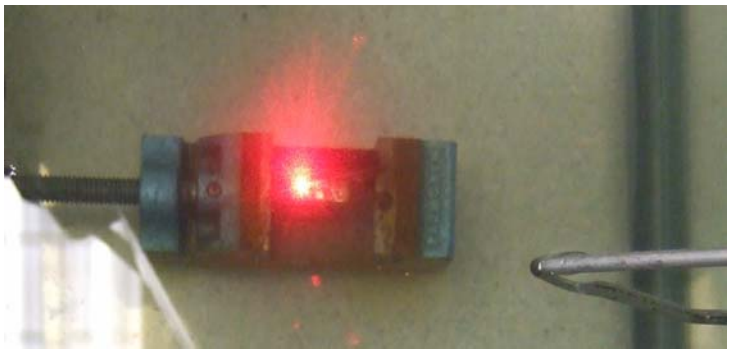

Figure 4.24 Packaged device held on the vice placed inside the water tank with laser on. A swath could be seen due to reflection of laser in water

Measuring the packaged membrane response in water was very challenging as the laser must pass through multiple layers before it reaches the membrane. These layers include the glass (container), water, PDMS, and silicone oil. This is possible, in theory, because all of these materials are transparent. However, when light is incident on any layer, it gets partly transmitted, partly absorbed, and partly reflected. As the light is absorbed by these layers, the intensity of the reflected beam drops making measurement difficult. On the other hand, if the light is reflected at the layer interfaces, there are multiple reflections besides the desired reflection from the membrane, which corrupts the measurements. Therefore, to minimize the layers of material through which laser must pass, the laser beam was passed through the top side of the tank there by eliminating the glass layer.

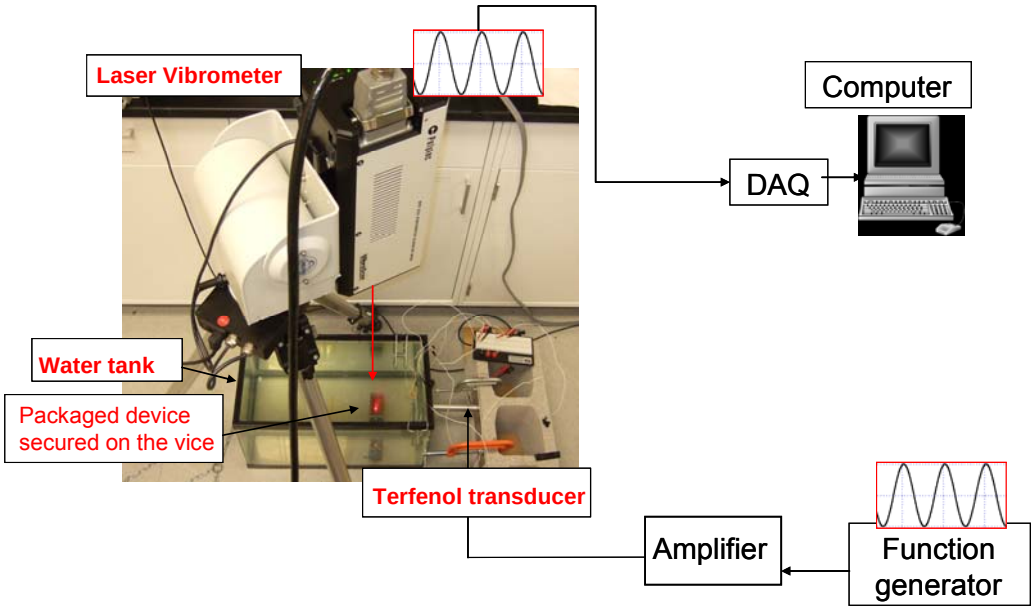

Figure 4.25 Flow chart showing the experiment setup for measuring the response of the packaged device inside water

The flowchart in Figure 4.25 shows the sequence for testing the packaged device inside water using the Laser Vibrometer. Again the frequency response was measured at two points on the device, one on the membrane and the other on the support, to calculate the transfer function between the support and the membrane. Since, the vice is now in contact with the glass tank, the lower frequencies (<2 kHz) were avoided because these vibrations displace the vice and hence shift the point of incidence of the laser beam.

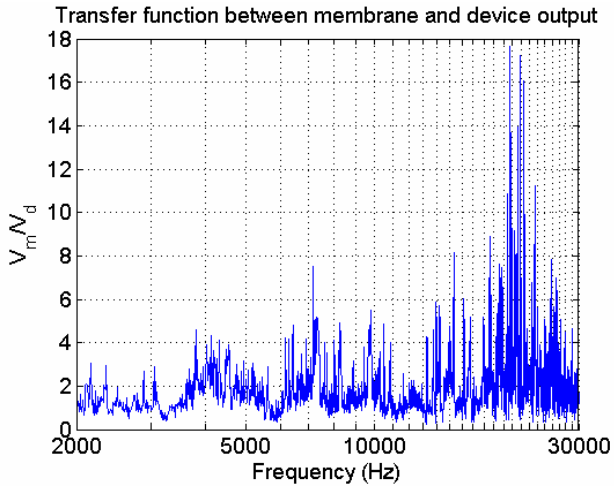

Figure 4.26 Transfer function between packaged membrane and device output in water

The transfer function between the device and the membrane is plotted in Figure 4.26. It can be seen that the data is very noisy owing to the fact that the laser beam has to still pass through water, PDMS, and silicone oil. It was observed that there were very strong reflections from the water surface and the PDMS. It was also observed that the reflected beam was wide spread and very low in intensity. All these factors resulted in the noisy data. However, it can still be seen that there is a peak at ~20 kHz, which established that the device (without nanowires) packaged in PDMS and silicone oil is responding to the acoustic waves.

5. CONCLUSION

A novel bio-inspired nanowire based acoustic sensor and its package have been designed for under-water applications utilizing the magnetostrictive properties of the smart material Galfenol ($Fe_{100-x}Ga_x$, where $15<x<28$). The sensor and its package mimic the structural design and the transduction process of a human-ear cochlea and were fabricated using micromachining techniques. Design efforts aimed at developing this acoustic transducer have been detailed in this thesis.

A silicon flexible membrane integrated with nanowires and a fixed membrane similar to the basilar membrane with cilia and the tectorial membrane in cochlea were designed. Magnetic properties and fabrication of nickel thin film has been studied to serve as a magnetic flux path between the nanowires and the GMR sensor for reducing flux leakage. Supermalloy which has better magnetic properties than nickel was also investigated. Its thin film was successfully deposited and patterned on a silicon nitride wafer, thus making it possible to utilize its magnetic properties to serve the purpose of a good magnetic flux path.

A small external package has been fabricated that incorporates impedance matching materials to allow sound waves to reach the acoustic sensor with minimal attenuation, while protecting it from the harsh under-water environment. It is also capable of resisting the ingression of moisture and salt ions that may corrode the Galfenol nanowires and other circuitry of the sensor. The acoustic impedance of candidate package materials was measured using scanning acoustic microscopy. Based on these measurements candidate

materials were chosen to optimize the impedance match with the seawater. Both PDMS with silicone oil and polyurethane with castor oil were found to be potential candidates for use as packaging materials. However, the advantage of PDMS is that it is transparent and possesses predefined micromachining processes, which would be helpful in integrating the packaging with the fabrication of the sensor in future. For this reason, PDMS was chosen to build a prototype package filled with silicone oil for the sensor.

A full process sequence for the fabrication of the sensor and its package is presented. Particular challenges related to wafer bonding, controlling membrane thickness, attaching nanowires to the membrane, wafer dicing, and device packaging were emphasized. The prototype device (without nanowires) was demonstrated to function both in air and in water. However, it is difficult to draw firm conclusions about sensor performance levels from the experiment, due to the limitation of the external testing equipment and the lack of the internal sensing mechanism (i.e. nanowires) in the sensor. Nevertheless, the fabrication of the miniaturized prototype of the sensor demonstrated that the process is practical for constructing a nanowire based acoustic sensor.

Device performance should be more conclusively tested when the GMR chip and the nanowires are integrated into a fully functioning sensor system. Successful operation of such a device offers particular benefits for SONAR applications and hearing implants, and will also help in further exploration of this acoustic transduction technology.

My Contributions

There are two facets of my contribution to this research project. One is the MEMS based design of the iron gallium nanowire acoustic sensor based on human ear cochlea and the other one is the packaging of the sensor for underwater applications. Both the design and packaging of the sensor are novel and have been developed for the first time.

I have designed an iron gallium nanowire based acoustic sensor that can be potentially used for SONAR. It is based on the structure design and transduction mechanism of the human ear cochlea. Micromachining techniques were successfully used to fabricate the miniaturized prototype sensor. My design of the acoustic sensor is to date the unique of its kind in the literature by incorporating nanowires mimicking the function of stereocilia. The design eliminated the nanowires to be frequency selective, which can be an issue during their fabrication. Experiment could not be performed on the device because nanowires were not available, but the testing of the basilar membrane in air was a promising start to the performance of the sensor. With the initial results and analytical calculations, it is expected that the basilar membrane would generate a stress of 600 MPa, giving a magnetic flux density change of 1.2 T, which can be easily measured by any magnetic sensor. This was not possible using nanowires alone in the acoustic sensor.

I have also addressed some important issues of incorporating a magnetic flux path for carrying the magnetic flux lines from the nanowires to the magnetic sensor with minimal losses. Experimental results demonstrated that nickel responds to the magnetic field and

can be used as a magnetic flux path. I kept the shape of the flux path either circular or elliptical to reduce the flux losses because of flux concentration at sharp corners.

I have developed the novel means of packaging the nanowire acoustic sensor for underwater applications that not only allows the sound waves to reach the sensor but also protects the delicate sensor from harsh underwater environment. I identified and evaluated the performance of the encapsulant and the fluid to be filled within the packaging cavity using scanning acoustic microscopy and acoustic testing. Experimental results helped predict that the sensor (although without nanowires) responds to the acoustic waves in water after packaging it with PDMS and silicone oil. I did the moisture absorption test for PDMS versus polyurethane both at room temperature and elevated temperature of 85ºC. The results indicated that moisture absorption for PDMS was less than that of the polyurethane. Even the accelerated moisture absorption test done for seven days showed that PDMS gained only 0.25% of weight compared to 3% weight gain by polyurethane when immersed in water. This is a very significant result in terms of the reliability of using PDMS as an encapsulant for packaging the sensor to be used for underwater applications.

Suggested future study

1. Currently the flexible membrane is a square membrane, which needs to be tapered like the life-size basilar membrane in the cochlea to make it frequency selective.
2. Supermalloy's magnetic properties need to be experimentally tested to check its suitability as the magnetic flux path between the nanowires and the GMR sensor.
3. It is also recommended to design the sensor with full mathematical modeling to obtain its optimal dimensions.
4. GMR chip needs to be integrated at the base of the nanowires, in order to eliminate the big commercially available GMR sensor and thus reduce the size of the sensor significantly.
5. Finally, the fabrication and packaging of the sensor needs to be integrated with the growing of the nanowires and the device should be tested as a whole.

APPENDIX A: MASKS

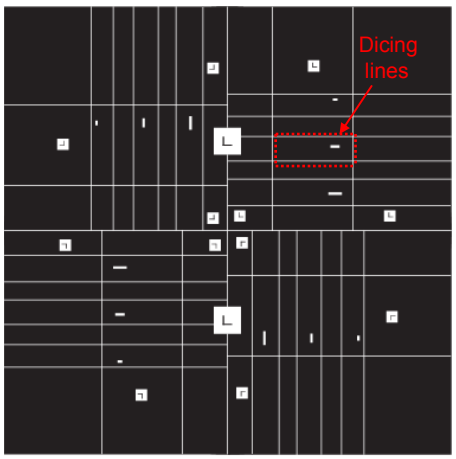

MASK 1 (top_etched channel)

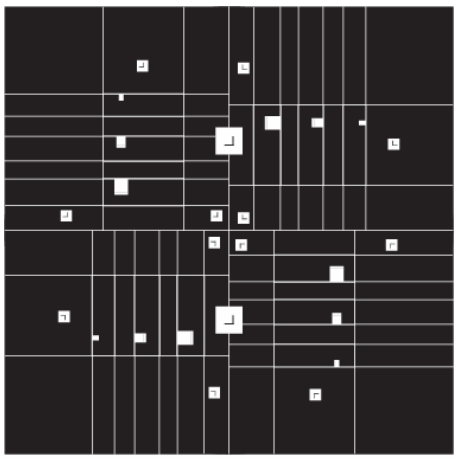

MASK 2,6 (bottom_membrane)

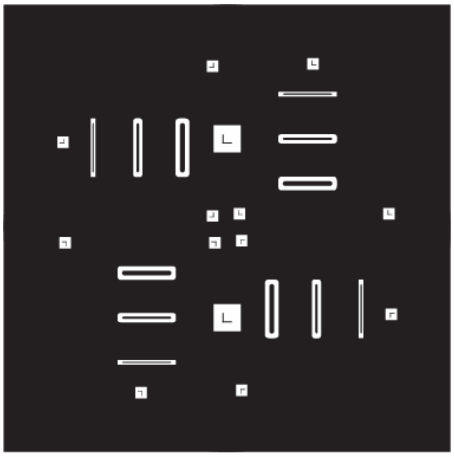

MASK 3 (top_partial etch)

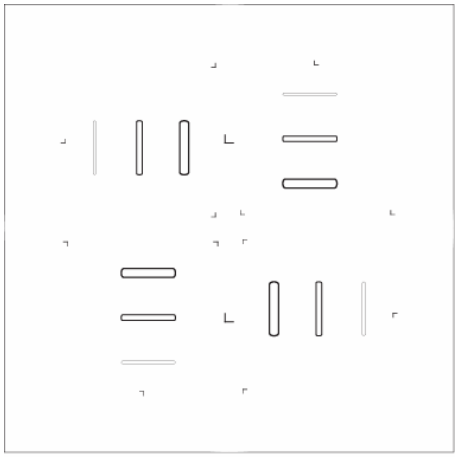

MASK 4 (top_nickel)

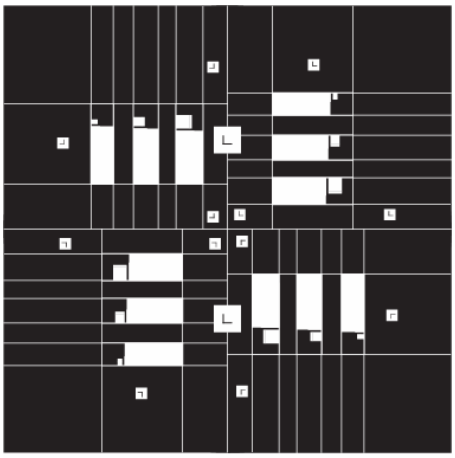

MASK 5 (top_for nanowires)

REFERENCES

[1] R. M. White, "Acoustic sensors for physical, chemical and biochemical applications," in *Proceedings of IEEE International Frequency Control Symposium*, Pasadena, CA, 1998, pp. 587-594.

[2] T. E. Bell, K. D. Wise, and D. J. Anderson, "A flexible micromachined electrode array for a cochlear prosthesis," in *Solid State Sensors and Actuators*, Chicago, IL, USA, 1997, pp. 1315-1318.

[3] G. Clark, R. S. C. Cowan, and R. C. Dowell, *Cochlear Implantation for Infants and Children*, First ed.: Singular, 1997.

[4] J. K. Shallop, A. Peterson, G. W. Facer, L. B. Fabry, and C. L. W. Driscoll, "Cochlear Implants in Five Cases of Auditory Neuropathy: Postoperative Findings and Progress," *Triological Society Papers, Laryngoscope,* vol. 111, No. 4, pp. 555-562, April 2001.

[5] G. T. Kovacs, *Micromachined Transducers Sourcebook*, 1 ed.: McGraw-Hill Science/Engineering/Math, 1998.

[6] P. D. McGary, L. Tan, J. Zou, B. J. H. Stadler, P. R. Downey, and A. B. Flatau, "Magnetic nanowires for acoustic sensors (Invited)," *Journal of Applied Physics,* vol. 99, 08B310, 2006.

[7] H. R. Schiffman, *Sensation and Perception: An Integrated Approach*. New York: John Wiley and Sons, Inc., 2001.

[8] "Sensitivity of Human Ear," url: http://hyperphysics.phy-astr.gsu.edu/hbase/sound/earsens.html.

[9] "ear, human.," in *Encyclopedia Britannica*, 2007.

[10] A. J. Hudspeth, "Mechanical amplification of stimuli by hair cells," *Curr. Opin. Neurobiol. ,* No. 7, pp. 480-486, 1997.

[11] P. C. Loizou, "Mimicking the human ear," *Signal Processing Magazine, IEEE,* vol. 15, No. 5, 1998.

[12] D. Haronian and N. C. MacDonald, Microelectromechanics-based frequency signature sensor, United States, Cornell Research Foundation, Inc. (Ithaca, NY), 5856722 http://www.freepatentsonline.com/5856722.html.

[13] S. Ando, K. Tanaka, and M. Abe, " Fishbone architecture: an equivalent mechanical model of cochleaand its application to sensors and actuators," in *International Conference on Solid State Sensors and Actuators*, Chicago, IL, USA, 1997, pp. 1027-1030.

[14] W. Hemmert, U. Durig, M. Despont, U. Drechsler, G. Genolet, P. Vettiger, and D. M. Freeman, "A life-sized hydrodynamical, micromechanical inner ear," in *Biophysics of the Cochlea: from Molecules to Models, A. W. Gummer, ed., World Scientific*, 2002, pp. 409-416.

[15] R. D. White, "Biomimetic trapped fluid microsystems for acoustic testing," Ph.D. thesis. University of Michigan, Ann Arbor, 2005.

[16] P. R. Scheeper, B. Nordstrand, J. O. Gullov, B. Liu, T. Clausen, L. Midjord, and T. Storgaard-Larsen, "A New Measurement Microphone Based on MEMS

Technology," *Journal of Microelectromechanical systems,* vol. 12, No. 6, pp. 880-891, December 2003.
[17] J. Bernstein, S. Finberg, K. Houston, L. Niles, H. D. Chen, L. E. Cross, K. K. Li, and K. Udayakumar, "Micromachined high frequency ferroelectric sonar transducers," *IEEE Transactions on Ultrasonics, Ferroelectrics, and Frequency Control,* vol. 44, No. 5, pp. 960–969, 1997.
[18] "Lateral line," url: http://en.wikipedia.org/wiki/Lateral_line.
[19] "Organ of Corti," url: http://hyperphysics.phy-astr.gsu.edu/hbase/sound/corti.html.
[20] "Hair Cell Orientation Patterns in Fish Saccules," url: http://www.life.umd.edu/biology/popperlab/background/orientation.htm.
[21] R. R. Fay and A. N. Popper, *Comparative Hearing: Fish and Amphibians*, First ed. New York: Springer, 1998.
[22] J. G. Benatar, "FEM implementations of magnetostrictive-based applications," M.S. thesis. University of Maryland, College Park, 2005.
[23] J. Atulasimha, "Characterization and Modeling of the Magnetomechanical Behavior of Iron-Gallium Alloys," PhD dissertation. University of Maryland, College Park, 2006.
[24] J. Atulasimha, A. B. Flatau, and R. A. Kellogg, "Sensing Behavior of Varied Stoichiometry Single Crystal Fe-Ga," *Journal of Intelligent Material Systems and Structures,* vol. 17, No. 2, pp. 97-105, February 1, 2006 2006.
[25] W. D. Armstrong, "Magnetization and magnetostriction processes in $Tb_{(0.27 - 0.30)}Dy_{(0.73 - 0.70)}Fe_{(1.9 - 2.0)}$," *Journal of Applied Physics,* vol. 81, No. 5, pp. 2321-2326, 1997.
[26] A. E. Clark, J. B. Restorff, M. Wun-Fogle, T. A. Lograsso, and D. L. Schalgel, "Magnetostrictive properties of body-centered cubic Fe-Ga and Fe-Ga-Al alloys," *IEEE Transactions on Magnetics,* vol. 36, pp. 3238-3240, 2000.
[27] R. A. Kellogg, A. B. Flatau, A. E. Clark, M. Wun-Fogle, and T. A. Lograsso, "Temperature and stress dependencies of the magnetic and magnetostrictive properties of $Fe_{0.81}Ga_{0.19}$," *Journal of Applied Physics* vol. 91, No. 10, pp. 7821-7823, May 15 2002.
[28] R. A. Kellogg, "Development and Modeling of Iron-Gallium Alloys," Ph.D thesis. Iowa State University, Iowa, Ames, 2003.
[29] P. R. Downey and A. B. Flatau, "Magnetoelastic bending of Galfenol for sensor applications," *Journal of Applied Physics,* vol. 97, No. 10, p. 10R505, 2005.
[30] P. D. McGary, L. Tan, and B. J. H. Stadler, "Engineering Magnetostrictive Heterostructures for Acoustic Cilia," in *US Navy Workshop on Acoustic Transduction Materials and Devices*, State College, PA, 2007.
[31] P. D. McGary and B. J. H. Stadler, "Electrochemical deposition of $Fe_{1-x}Ga_x$ nanowire arrays," *Journal of Applied Physics,* vol. 97, 10R503, 2005.
[32] J. Zou, X. Qi, L. Tan, and B.J.H.Stadler, "Nanoporous Silicon with Long-Range-Order using Imprinted Anodic Alumina Etch Masks," *Applied Physics Letters,* vol. 89, 093106, 2006.
[33] L. Tan and B. J. H. Stadler, "Fabrication and Magnetic Behavior of Co/Cu Multilayered Nanowires," *Journal of Materials Research,* vol. 21 no.11, pp. 2870-2875, 2006.

[34] C. Mudivarthi and A. B. Flatau, "Modeling of fluid-structure interaction for nanoscale acoustic transducer," in *US Navy Workshop on Acoustic Transduction Materials and Devices*, State College, PA, 2006.
[35] A. Guyton, *Textbook of Medical Physiology*. Philadelphia: WB Saunders, 1976.
[36] W. H. Xu and T. Y. Zhang, "Mechanical characterization of trilayer thin films by the microbridge testing method," *Applied Physics Letters,* vol. 83, No. 9, pp. 1731-1733, 2003.
[37] M. Martyniuk, J. Antoszewski, C. A. Musca, J. M. Dell, and L. Faraone, "Stress in low-temperature plasma enhanced chemical vapor deposited silicon nitride thin films," *Smart Materials and Structures,* vol. 15, pp. S29–S38, 2006.
[38] S. Chikazumi, *Physics of Magnetism*: John Wiley and Sons, Inc., Library of Congress Catalog Card No 64-14985, 1964.
[39] J. Daughton and Y. Chen, "GMR Materials for Low Field Applications," in *IEEE Transactions on Magnetics*, 1993, pp. 2705-2710.
[40] J. Daughton, J. Brown, E. Chen, R. Beech, A. Pohm, and W. Kude, "Magnetic Field Sensors Using GMR Multilayer," *IEEE Transactions on Magnetics,* vol. 30, No. 6, pp. 4608-4610, November 1994.
[41] R. W. Schneider and C. H. Smith, "Low Magnetic Field Sensing with GMR Sensors, Part I: The Theory of Solid-State Magnetic Sensing," in *Sensors*, 1999.
[42] C. Tsang, R. E. Fontana, T. Lin, D. E. Heim, V. S. Speriosu, B. A. Gurney, and M. L. Williams, "Design, fabrication and testing of spin-valve read heads for high density recording," *IEEE Transactions on Magnetics,* vol. 30, No. 6, pp. 3801-3806, 1994.
[43] P. Downey, R. Jain, C. Mudivarthi, and A. Flatau, "Nanowire Applications: Characterization and Fabrication of Acoustic Sensors " in *ONR MURI Review,* Penn State, PA, 2007.
[44] M. M. C. Kazuhiro Hono, National Institute for Materials Science (NIMS), "Ferromagnetic materials," 2006. URL: http://www.nims.jp/apfim/pdf/MMC_Lecture6.pdf.
[45] R. M. Bozorth, *Ferromagnetism (I), Chapter 5, pp 102-189*. New York: Wiley-IEEE Press, 1993.
[46] H. A. Yang, C. W. Lin, C. Y. Peng, and W. Fang, "On the selective magnetic induction heating of micron scale structures," *Journal of Micromechanics and Microengineering,* vol. 16, pp. 1314-1320, 2006.
[47] "Thermionics Laboratory Inc.," url: http://www.thermionics.com/download/evaprate.pdf.
[48] E. P. Furlani, *Permanent Magnet and Electromechanical Devices: Materials, Analysis, and Applications*: Elsevier, 2001.
[49] J. Y. Park, S. H. Han, W. P. Taylor, and M. G. Allen, "Fully integrated micromachined inductors with electroplatedanisotropic magnetic cores," in *Thirteenth Annual Conference Proceedings on Applied Power Electronics Conference and Exposition*, 1998, pp. 379-385.
[50] L. Warren and J. R. Paterson, "The use of thermal imaging for the development of materials towithstand extreme service conditions," in *Dielectric Materials, Fifth International Conference on Measurements and Applications*, Canterbury, UK, 1988, pp. 290-292.

[51] R. J. DiSabatino, "Packaging of an Iron-Gallium Nanowire Acoustic Sensor," M.S. thesis. University of Maryland, College Park, 2006.
[52] "MSDS Silicone Oil," Catalog No. S159-500.
[53] *CRC Handbook of Chemistry and Physics*. Cleveland, Ohio: CRC Press, 2004.
[54] A. Tamburrano and M. S. Sarto, "Electromagnetic characterization of innovative shielding materials in the frequency range up to 8 gigahertz," *International Symposium on Electromagnetic Compatibility,* vol. 2, pp. 551-556, Aug 9-13 2004.
[55] D. L. Smith, *Thin-film deposition: Principles and Practice*. New York: McGraw Hill Inc., 1995.
[56] H. Yang, R. F. Pinizzotto, L. Luo, and F. Namavar, "Microstructural analysis of nickel silicide formed by nickel/silicon-on-oxide annealing," *Applied Physics Letters,* vol. 62, No. 21, pp. 2694-2696, 1993.